

1     **Shear wave velocity structure beneath Northeast China from joint inversion of**  
2             **receiver functions and Rayleigh wave group velocities: Implications for**  
3                     **intraplate volcanism**

4     *Zheng Tang<sup>1, \*</sup>, Jordi Julià<sup>2</sup>, P. Martin Mai<sup>3</sup>, Walter D. Mooney<sup>4</sup>, and Yanqiang Wu<sup>1</sup>*

5     <sup>1</sup>*The First Monitoring and Application Center, China Earthquake Administration, Tianjin,*  
6     *China*

7     <sup>2</sup>*Departamento de Geofísica, Universidade Federal do Rio Grando do Norte, Natal, Brazil*

8     <sup>3</sup>*Earth Science and Engineering Program, King Abdullah University of Science and*  
9     *Technology, Thuwal, Saudi Arabia*

10    <sup>4</sup>*Earthquake Science Center, United States Geological Survey, Menlo Park, California, United*  
11    *States*

12    **Key Points**

- 13       ● A low S-velocity belt related to Cenozoic volcanism and fast S-velocity  
14       anomalies interpreted as mafic intrusions are observed in the crust.
- 15       ● A high S-velocity anomaly may infer a depleted and refractory lithosphere,  
16       inducing the absence of Cenozoic volcanism in the Songliao basin.
- 17       ● The lithosphere is 50-70 km thick below the Changbai mountains and thickens  
18       westward to >125 km beneath the Greater Xing'an mountain range.

19    **Abstract**

20       A high-resolution 3-D crustal and upper-mantle shear-wave velocity model of  
21    Northeast China is established by joint inversion of receiver functions and Rayleigh  
22    wave group velocities. The teleseismic data for obtaining receiver functions are  
23    collected from 107 CEA permanent sites and 118 NECESSArray portable stations.

24 Rayleigh wave dispersion measurements are extracted from an independent  
25 tomographic study. Our model exhibits unprecedented detail in S-velocity structure.  
26 Particularly, we discover a low S-velocity belt at 7.5-12.5 km depth covering entire  
27 Northeast China (except the Songliao basin), which is attributed to a combination of  
28 anomalous temperature, partial melts and fluid-filled faults related to Cenozoic  
29 volcanism. Localized crustal fast S-velocity anomaly under the Songliao basin is  
30 imaged and interpreted as late-Mesozoic mafic intrusions. In the upper mantle, our  
31 model confirms the presence of low velocity zones below the Changbai mountains and  
32 Lesser Xing'an mountain range, which agree with models invoking sub-lithospheric  
33 mantle upwellings. We observe a positive S-velocity anomaly at 50-90 km depth under  
34 the Songliao basin, which may represent a depleted and more refractory lithosphere  
35 inducing the absence of Cenozoic volcanism. Additionally, the average lithosphere-  
36 asthenosphere boundary depth increases from 50-70 km under the Changbai mountains  
37 to 100 km below the Songliao basin, and exceeds 125 km beneath the Greater Xing'an  
38 mountain range in the west. Furthermore, compared with other Precambrian  
39 lithospheres, Northeast China likely has a rather warm crust (~480-970 °C) and a  
40 slightly warm uppermost mantle (~1200 °C), probably associated with active  
41 volcanism. The Songliao basin possesses a moderately warm uppermost mantle (~1080  
42 °C).

### 43 **Plain Language Summary**

44 Northeast China is a unique region with a combination of ancient Precambrian  
45 geology and active seismicity and volcanism. The presence of widely distributed  
46 volcanoes in this region is enigmatic and their origin has been widely debated. We use  
47 available seismic data to create a high-resolution 3-D S-wave seismic velocity model

48 for the crust and upper mantle of Northeast China. Our model reveals significant multi-  
49 scale low and high velocity anomalies in the crust, mantle lithosphere and  
50 asthenosphere that we associate with the volcanic/magmatic processes. The lithospheric  
51 thickness gradually increases from 50-70 km beneath the Changbai mountains to >125  
52 km some 1,000 km to the west. Our results provide novel constraints on the crustal and  
53 upper-mantle structure of Northeast China and help to interpret the mechanism behind  
54 volcanism and the geodynamics.

55 **Keywords:** receiver function, joint inversion, shear-wave velocity, intraplate  
56 volcanism, Songliao basin, Northeast China

## 57 **1. Introduction**

58 Northeast China (Figure 1a) is situated along the eastern margin of the  
59 Xingmeng Orogenic Belt, which is surrounded by the Siberian craton to the north, the  
60 North China craton to the south, and the subducting Pacific plate to the east (Şengör et  
61 al., 1993). This region was formed by the amalgamation of a series of accretionary  
62 wedges and micro-blocks (Ge & Ma, 2007; Zhou & Wilde, 2013). Since the late  
63 Mesozoic, the Pacific slab westward subduction has played a major role in the tectonic  
64 setting and evolution of Northeast China (Deng et al., 1996; Wu et al., 2003). Intensive  
65 extensional deformation, along with extensive intraplate volcanism (Wu et al., 2005;  
66 Zhang et al., 2010) and development of rift basins (Meng, 2003; Wei et al., 2010),  
67 occurred in the area, possibly triggered by the rollback of the Paleo-Pacific slab during  
68 the late Jurassic to early Cretaceous (Wang et al., 2006; Wu et al., 2005).

69 Volcanism in Northeast China has been continuously active during the  
70 Cenozoic. Volcanic rocks are spatially distributed along the three belts making up  
71 Northeast China: the Changbai mountains (CBM), the Lesser Xing'an mountain range

72 (LXM), and the Greater Xing'an mountain range (GXM), which bound the Songliao  
73 basin (SLB) in the center (Fan & Hooper, 1991; Liu, 1987; Liu et al., 2001). Among  
74 hundreds of Cenozoic volcanoes, prominent ones include Changbaishan and Jingpohu  
75 volcanoes in the east, Wudalianchi volcano in the north, and Halaha and Abaga  
76 volcanoes in the western inland (Figure 1a).

77         One popular geodynamic model proposes, based on mantle tomography, that  
78 Cenozoic volcanism in Northeast China is induced by the stagnation and deep  
79 dehydration of the subducted Pacific plate in the mantle transition zone (Ma et al., 2018;  
80 Tian et al., 2016; Wei et al., 2012, 2015, 2019; Zhao et al., 2004, 2009, 2012). The  
81 Pacific westward subduction and stagnation in the mantle transition zone may have  
82 resulted in a big mantle wedge above the subducted slab (Zhao et al., 2009, 2012). The  
83 stagnant slab in the mantle transition zone would then continuously release fluids to the  
84 big mantle wedge, leading to hot and wet mantle upwellings under Northeast China  
85 (Ohtani et al., 2004; Zhao & Ohtani, 2009; Zhao et al., 2009). However, the spatial  
86 distribution of the volcanism – volcanoes in the western interior are at least hundreds  
87 of kilometers away from those in the east, while the SLB in the center manifests an  
88 absence of Cenozoic volcanism – make it difficult to believe that all the volcanoes in  
89 Northeast China followed the same formation mechanism (i.e., hot mantle upwelling  
90 across a big mantle wedge). Although Cenozoic volcanic activity within a given  
91 subregion might have a common origin or be associated with other subregions at deep  
92 mantle levels, it seems more likely that each have their own characteristics and  
93 geodynamic histories.

94         Another model suggests that, although still related to deep subduction processes,  
95 volcanism in the CBM region is driven by an upwelling of sub-slab mantle materials

96 through a gap in the stagnant Pacific slab (Tang et al., 2014). Both the joint inversion  
97 of Rayleigh wave phase velocity dispersion and S-wave travel times (Guo et al., 2018)  
98 and the full waveform mantle tomography carried out by Tao et al. (2018) resolve a  
99 cylindrical slow velocity anomaly through the mantle transition zone roughly below the  
100 CBM region, which is consistent with the above hypothesis above (i.e., mantle  
101 upwelling through a slab gap). Additionally, the surface wave tomography of Guo et  
102 al. (2016) suggested a mantle convection model in which the mantle upwelling beneath  
103 the CBM would induce a downwelling return flow under the SLB. This downwelling  
104 would in turn trigger local mantle upwellings below the Halaha and Abaga volcanoes  
105 in the west. Although this “mantle upwelling through a slab gap and associated mantle  
106 convection” model suggests potential correlations and differences in formation  
107 mechanisms among the volcanoes, it does not account for the presence of the  
108 Wudalianchi volcano in the northern region. Thus, this model requires additional  
109 constraints before it can become a viable geodynamic model for Northeast China.

110 Previous studies have investigated the deep crustal and mantle structure of  
111 Northeast China. Large-scale body wave travel-time tomography (e.g., Huang & Zhao,  
112 2006; Lei & Zhao, 2005; Li & Van der Hilst, 2010; Ma et al., 2018; Tang et al., 2014;  
113 Wei et al., 2012, 2015; Zhang, Wu, & Li, 2013; Zhao et al., 2009; Zhao & Tian, 2013)  
114 reported a significant upper-mantle low velocity anomaly down to ~400 km depth  
115 below the CBM, a broad high velocity zone that is likely associated with the subducted  
116 Pacific slab at the mantle transition zone depths, and possible low velocity anomalies  
117 in the asthenospheric mantle roughly beneath the Halaha and Abaga volcanic fields. As  
118 mentioned above, Tang et al. (2014) imaged a debated feature: a cylindrical low  
119 velocity anomaly rising through the mantle transition zone under the CBM region.  
120 Surface wave tomography (e.g., Fan et al., 2020, 2021; Guo et al., 2016; Li et al., 2012,

121 2013; Pan et al., 2014, 2015) found a low velocity feature at lower-crustal depths under  
122 the CBM, upper-mantle low S-velocities and extremely thin lithosphere beneath the  
123 CBM, LXM and Sanjiang basin. Receiver function studies (e.g., He et al., 2013; Liu &  
124 Niu, 2011; Tao et al., 2014; Zhang et al., 2014; Zhang, Wu, Pan, et al., 2013)  
125 constrained crustal thicknesses and bulk Vp/Vs ratios across Northeast China, with  
126 crustal thicknesses ranging between 26 and 42 km while bulk Vp/Vs ratios varied  
127 between 1.60 and 1.88 (He et al., 2013; Tao et al., 2014). Tao et al. (2014) highlighted  
128 isostatic anomalies in the eastern margin of the SLB, the CBM, and the southern GXM.  
129 Guo et al. (2015) exhibited high S-velocities in the crust below the SLB. Local  
130 geophysical imaging (e.g., Hammond et al., 2019; Gao et al., 2020; Li et al., 2016; Tang  
131 et al., 2001; Zhan et al., 2006; Zhang et al., 2002) showed low-velocity and low-  
132 resistivity bodies underneath the Wudalianchi and Changbaishan volcanoes, inferring  
133 possible crustal magma chambers or partial melts.

134         Although these studies provide robust geophysical constraints in interpreting  
135 the mechanism of intraplate volcanism and the tectonic evolution of Northeast China,  
136 important details in structure, particularly fine shear-wave velocity variations at crustal  
137 and lithospheric mantle levels, remain ambiguous. Large-scale body-wave travel-time  
138 and surface wave tomography studies do not resolve lithospheric details due to the very  
139 nature of the datasets. Previous investigations with receiver functions are limited by  
140 sparse distribution of stations. Imaging these detailed structures in the crust and  
141 lithospheric mantle is thus essential for understanding the correlations and differences  
142 among the volcanoes of Northeast China and correctly interpreting their emplacement  
143 mechanisms.

144         In this study, we develop a high-resolution 3-D shear-wave velocity model for

145 Northeast China using data from a dense seismic experiment. We take advantage of  
146 constraints from both receiver functions and surface wave dispersion velocities, which  
147 are sensitive to relative variations in velocity structure and absolute background  
148 velocities, respectively. A joint inversion of receiver functions and fundamental-mode  
149 Rayleigh wave group velocities was performed at each station, so our results map multi-  
150 scale S-velocity anomalies and provide novel constraints on the crustal and uppermost-  
151 mantle structure. These constraints help in turn to interpret the mechanism behind  
152 intraplate volcanism and the geodynamics of Northeast China.

## 153 **2. Seismic Data**

154 The datasets utilized in this study were assembled from a total of 225 broadband  
155 stations in Northeast China (Figure 1b). Up to 107 of these stations were part of the  
156 permanent China Digital Seismic Network (ChinaNetwork, 2006) and were operated  
157 by the China Earthquake Administration (CEA), while the other 118 sites belonged to  
158 the Northeast China Extended Seismic Station Array (NECESSArray), deployed from  
159 September 2009 to August 2011. The temporary network NECESSArray improves the  
160 spatial station coverage south of  $\sim 48^\circ\text{N}$ , where the station distribution is more even and  
161 inter-station distances remain less than 70 km. For the 107 CEA sites, over 700  
162 teleseismic events, with epicentral distances between  $30^\circ$  and  $90^\circ$  and body-wave  
163 magnitudes above 5.5 within a four-year period (2016-2019) were selected to compute  
164 receiver functions (Figure S1a). For the 118 NECESSArray stations, more than 600  
165 events within the same distance range and magnitude threshold between September  
166 2009 and August 2011 were collected (Figure S1b). Note that the selected time  
167 windows for each network do not overlap; nonetheless, the spatial distribution of  
168 earthquakes recorded by each network is quite similar, with concentration of epicenters

169 along the Mediterranean-Iran-Himalaya belt, the circum-Indian belt, and the circum-  
170 Pacific belt (e.g., Mariana and Aleutian Islands).

## 171 **2.1. Receiver Functions**

172 Receiver functions are time series that carry information about the seismic  
173 velocity structure underlying the recording station (Langston, 1979). The time series  
174 can be regarded as source-equalized seismic waveforms composed of the direct P wave  
175 and secondary phases triggered by the interaction of an incoming P wavefront with  
176 near-station subsurface discontinuities. For each discontinuity, the secondary arrivals  
177 mainly comprise a P-to-S conversion upon refraction across the interface (Ps) and two  
178 multiples reverberating between the free surface and the discontinuity (PpPs and PpSs  
179 + PsPs). The seismic velocity variations with depth below the recording station can be  
180 determined by modeling the relative travel-times and amplitudes making up the receiver  
181 function waveforms (Ammon et al., 1990; Owens et al., 1984).

182 Receiver functions are estimated by deconvolving the vertical component of  
183 teleseismic P wave recordings from the corresponding horizontal components. For that  
184 purpose, we applied a time domain iterative deconvolution technique (Ligorria &  
185 Ammon 1999) with 500 iterations. Before deconvolution, we windowed the three-  
186 component seismograms 10 s prior to the P wave arrival and 110 s after, demeaned,  
187 detrended, tapered and band-pass filtered the traces between 0.05 and 4 Hz to prevent  
188 low- and high-frequency noise and aliasing. Subsequently, we down-sampled the  
189 filtered waveforms to 10 samples per second and rotated the horizontal components  
190 around the vertical component into the great-circle path to determine the corresponding  
191 radial and transverse traces. Finally, both radial and transverse receiver functions were  
192 obtained by deconvolving the vertical component from the radial and transverse

193 components, respectively. Although the transverse receiver functions were not included  
194 during the analysis, they help to assess lateral heterogeneities and anisotropy of the  
195 subsurface (Savage, 1998). In addition, we employed a Gaussian low-pass filter to limit  
196 the frequency content of the deconvolved traces. For each event, receiver functions in  
197 both the high ( $f_c \leq 1.25$  Hz, Gaussian width  $\alpha = 2.5$ ) and low ( $f_c \leq 0.50$  Hz, Gaussian  
198 width  $\alpha = 1.0$ ) frequency bands were obtained for the subsequent joint inversion, as  
199 they contain information on velocity heterogeneities at different scales and help to  
200 distinguish velocity jumps from gradational transitions (Julià, 2007).

201       Following Tang et al. (2016, 2019), a two-step quality control was employed to  
202 retain high-quality receiver functions. First, receiver functions that did not reproduce at  
203 least 85% of the horizontal traces when convolved back with the corresponding vertical  
204 seismograms were rejected. Second, we visually examined transverse receiver function  
205 waveforms and those with abnormally large amplitudes in the transverse component  
206 were disregarded. As mentioned above, large transverse amplitudes may result from  
207 lateral heterogeneities and/or anisotropy (Savage, 1998) but may also indicate failure  
208 during rotation into the great circle path. Unstable and extremely distorted radial  
209 receiver functions were also visually removed from the dataset. Overall, from the  
210 permanent CEA network, a total of 16,848 radial receiver functions in the high-  
211 frequency band ( $f_c \leq 1.25$  Hz) and 16,096 radial receiver functions in the low-frequency  
212 range ( $f_c \leq 0.50$  Hz) were kept from the initial selection of 63,838 seismograms.  
213 Additionally, 12,135 radial receiver functions at Gaussian width of  $\alpha = 2.5$  and 11,796  
214 receiver functions at Gaussian parameter of  $\alpha = 1.0$  from the temporary NECESSArray  
215 stations were accepted after our quality control, out of a total of 59,919 teleseismic  
216 waveforms.

217 Receiver function waveforms recorded by some stations in sedimentary basins  
218 are sometimes dominated by high-amplitude, low-frequency ringy signals that result  
219 from seismic energy reverberating in the low-velocity sedimentary layer. The  
220 reverberations may partially or totally mask the P-to-S conversions generated at deep  
221 seismic interfaces, making it difficult to extract structural information from deep crustal  
222 or upper-mantle levels (e.g., Julià et al., 2004; Zelt & Ellis, 1999). We therefore applied  
223 a resonance removal filter (Yu et al., 2015) on those receiver functions to effectively  
224 eliminate or significantly reduce the multiples associated with low-velocity sediments,  
225 but keeping the primary P-to-S conversion generated at the sediment-bedrock interface.  
226 The basic idea is to apply a frequency-domain filter of the form  $(1 + r_0 e^{-i\omega\Delta t})$  to the  
227 original receiver function, where the strength of the near-surface reverberations ( $r_0$ ) and  
228 the two-way traveltimes ( $\Delta t$ ) for the reverberations are determined from the normalized  
229 autocorrelation function. An example performing the resonance removal filter with real  
230 data recorded by station NEA7 is shown in Figure S2. Note that the original receiver  
231 functions in both frequency bands (Figure S2a, b) at NEA7 are ringy. After the  
232 resonance removal filter, the ringing components of the signal are effectively reduced  
233 in the deconvolved traces (Figure S2c, d). Additionally, a synthetic test (Figures S3-  
234 S5) demonstrates that the resonance removal filter effectively removes the multiples of  
235 converted shear waves within sedimentary layer and successfully recovers the desired  
236 P-to-S signals generated at deep discontinuities in both lag time and amplitude.

237 Subsequently, for each station and Gaussian width, we grouped receiver  
238 functions from similar directions (i.e., back-azimuth) and comparable epicentral  
239 distances (i.e., ray-parameter) into bins to then average them. Within each bin, we  
240 constrained the maximum deviations in ray-parameter and back-azimuth to no more  
241 than 0.01 s/km and  $10^\circ$ , respectively. Every bin was composed of at least 3 deconvolved

242 traces. Therefore, several receiver function averages with different average back-  
243 azimuths and ray-parameters were obtained for each station, sampling the Earth in  
244 various directions at each recording site to reflect the effects of azimuthal variations.  
245 Figure 2 exhibits selected radial receiver function averages at both Gaussian widths for  
246 a few stations. Generally, the time series reveal clear Ps conversions and reverberations  
247 due to the Moho discontinuity. At some sites (e.g., NE38, NE68, NE78, NEA6, NEA7,  
248 and NEAB), the receiver function averages are the result of applying the resonance  
249 removal filter mentioned above.

## 250 **2.2. Rayleigh Wave Group Velocities**

251 An independent tomographic study carried by Li et al. (2013) provided local  
252 Rayleigh wave group velocities for each station. Li et al. (2013) measured fundamental-  
253 mode Rayleigh wave group velocities from earthquakes that are mostly located on the  
254 circum-Pacific belt, the circum-Indian belt and western China. They compiled  
255 observations from permanent stations operated by CEA in mainland China and  
256 temporary arrays (e.g., GEOSCOPE, KNET, and KZNET) deployed in adjacent areas.  
257 They performed single-station measurements of group velocity applying a wavelet  
258 transformation frequency-time analysis method (Wu et al., 2009). Rayleigh wave  
259 dispersion curves were acquired at periods between 10 and 145 s along more than 9,500  
260 paths across the entire East Asia region. Subsequently, Rayleigh wave group velocities  
261 were tomographically inverted on a 2-D rectangular grid with node spacing of  $1^\circ$  in  
262 both latitude and longitude. The best resolution of their 2-D group velocity maps for  
263 the majority of East Asia is roughly  $3^\circ$  according to checkerboard tests (Li et al., 2013).

## 264 **3. Joint Inversion**

265 Receiver functions are usually inverted for shear wave velocity structure,

266 although they are also theoretically sensitive to compressional wave velocities and  
267 densities (Owens et al., 1984). Previous studies illustrated that the main sensitivity of  
268 receiver function is to relative velocity contrasts and vertical S-P travel-times, not to  
269 absolute vertical S-velocities (Ammon et al., 1990). Thus, receiver functions can  
270 resolve small-scale relative shear-wave velocities, but the inverse problem is non-  
271 unique. Surface wave dispersion curves, in contrast, constrain averages of absolute S-  
272 velocities within frequency-dependent depth-ranges, although the wavelengths  
273 associated with surface waves cannot resolve small-scale variations (Julià et al., 2000).  
274 Therefore, we take advantage of the complementarity of receiver functions and surface  
275 wave dispersions to jointly invert both datasets, so that the inverted models reflect  
276 average background velocities constrained by the dispersion data with the details from  
277 the receiver function dataset superimposed. Moreover, the non-uniqueness of receiver  
278 function inversion is significantly reduced with the addition of surface wave dispersion  
279 measurements (Julià et al., 2000).

### 280 **3.1. Joint Inversion Details**

281 Applying the linearized scheme of Julià et al. (2000, 2003), we conducted the  
282 joint inversion of receiver functions and Rayleigh wave group velocities to obtain a  
283 shear-wave velocity-depth profile of the crust and upper mantle at each station.  
284 Conceptually, the joint inversion summarizes the structural information contained in  
285 both receiver function and dispersion curve into a simplified 1-D Earth model. To  
286 equalize the contributions from each dataset, both sets of observations are normalized  
287 by the number of data points and the corresponding physical units (Julià et al., 2000).  
288 Also, an *a priori* factor that controls the relative influence of each dataset into the joint  
289 inversion is employed. We chose 0.5 for this parameter to give equal weight to each

290 dataset in our calculations. In addition, the inversion employs a depth-dependent  
291 smoothing on the velocity-depth profiles, which allows rapid perturbations of shear-  
292 wave speed at shallow layers (i.e., 0–55 km depths) but suppresses large velocity  
293 variations at deep levels (i.e., below 55 km depth). The smoothness constraint consists  
294 of minimizing the second velocity differences among adjacent model layers. A  
295 smoothness factor, which controls the trade-off between model smoothness and  
296 matching the observations, was set to be 0.2 after trial and error.

297         The model is parameterized in terms of homogeneous horizontal layers with  
298 fixed thickness and velocity. Layer thicknesses are 2.5 km at depths of 0–60 km, 5 km  
299 at 60–150 km, and 10 km under 150 km depth (maximum depth considered: 400 km).  
300 The P-wave velocity is estimated by assuming a constant  $V_p/V_s$  ratio (1.75 for 0–40 km  
301 depths; 1.81–1.85 for 40-km-depth below) for each layer. Density is inferred from the  
302 resulting compressional velocity through the empirical relation of Berteussen (1977).  
303 The initial model needed for the linearized joint inversion comprises a 40 km thick crust  
304 with gradually increasing S-velocities from 3.4 to 4.0 km/s and a flattened PREM  
305 (Preliminary reference Earth model) upper mantle (Dziewonski & Anderson, 1981).

306         Sedimentary structure generally leads to complex receiver function waveforms,  
307 despite a resonance removal filter being applied to eliminate or suppress the near-  
308 surface reverberations. For stations situated on sediments, we found it necessary to  
309 guide the joint inversion through the inclusion of a near-surface layer with slow  
310 (sediment like) velocities in the starting model. For those stations, we tested different  
311 thickness of the near-surface layer (i.e., 1.0, 1.5, 2.0, and 2.5 km) and used a  
312 sedimentary shear-wave velocity of 1.71 km/s in all cases. Also, a stronger smoothness  
313 constraint (i.e., 0.5) was required to prevent numerical instabilities during the inversion

314 process.

315 We inverted for S-wave velocities only above 270 km depth, although the model  
316 was parameterized down to the bottom of the upper mantle (400 km depth). The  
317 approach of Julià et al. (2000, 2003) allows fixing the S-wave velocities of given layers  
318 to predetermined values by applying an extremely high weight for those layers. For the  
319 deep levels below 270 km depth, shear velocities were forced to be PREM-like during  
320 the inversion, thus accounting for the partial sensitivity of long-period dispersion  
321 velocity to deep Earth structure (Julià et al., 2003, 2009).

### 322 **3.2. Shear Wave Velocity Profiles and Uncertainties**

323 We obtained shear-wave velocity-depth profiles at 225 stations by jointly  
324 inverting the receiver functions with local Rayleigh wave group velocities. Figure 3  
325 presents the joint inversion for the permanent station WDL situated on the LXM (the  
326 location is marked in Figure 2). For this case, a total of 13 receiver function averages,  
327 which sample the subsurface from various directions (i.e., average back-azimuths  
328 between  $43^\circ$  and  $310^\circ$ ) and different incident angles (i.e., average ray-parameters of  
329 0.044-0.077 s/km), were computed in both the high- and low-frequency bands. All  
330 average waveforms, particularly the prominent Ps conversion and two multiples from  
331 the Moho discontinuity, are consistently observed at similar lag times. This indicates  
332 that the Earth structure underlying the station can be successfully modelled through a  
333 single 1-D velocity-depth profile, although some small-scale azimuthal variations may  
334 exist. Both the predicted receiver function and dispersion data match the corresponding  
335 observations very well. The resulting 1-D model shows a 30 km thick crust consisting  
336 of an upper crust with S velocities of 3.3–3.4 km/s down to 12.5 km and a lower crust  
337 with shear velocities of 3.5–3.7 km/s at 12.5–30 km depth. The Moho interface is sharp

338 and located at 30 km depth. In the upper mantle, a low velocity anomaly with shear-  
339 wave speeds of 4.2–4.3 km/s between 40 and 60 km depth and a low velocity zone  
340 starting roughly at 100 km depth are imaged.

341 Another example is displayed in Figure 4 for the temporary station NE4A in the  
342 CBM region (the location is shown in Figure 2). A total of 11 receiver function groups  
343 were formed, with ray-parameters between 0.045 and 0.075 s/km and back-azimuths in  
344 the 55°–230° range. As before, an average 1-D velocity-depth profile was inverted from  
345 all receiver function averages and dispersion velocities. The model reveals a sharp  
346 Moho at 32.5 km depth. Above the Moho, the crust consists of a 12.5 km thick upper  
347 crust with a possible low velocity zone at 7.5–12.5 km depth, a middle crust with  
348 gradually increasing S-wave velocities from ~3.6 to ~3.8 km/s between 12.5 and 27.5  
349 km depth, and a fast-velocity lower crust with shear velocities of 3.9–4.1 km/s at 27.5–  
350 32.5 km depths. The upper mantle contains a very thin lid of ~7.5 km followed by slow  
351 velocities down below. Particularly, below ~85 km depth, S-wave velocities slower  
352 than 4.25 km/s are revealed.

353 As mentioned in section 3.1, for a few sites that overlie sediments, we performed  
354 several joint inversions in order to test different sedimentary layer thicknesses and  
355 obtain a solution that best matched the receiver function waveforms. To that effect, we  
356 divided the top 2.5-km of the general starting model into two layers: an uppermost layer  
357 with a sediment-like S-wave velocity of 1.71 km/s, and a lowermost layer with a more  
358 crystalline-basement velocity of 3.42 km/s. The thickness of the sediment was set to  
359 1.0, 1.5, 2.0, and 2.5 km, successively. An example for station NEA6 (in the SLB, see  
360 Figure 2) illustrating the above procedure is provided in the supplementary document  
361 (Figures S6–S10). Without considering sedimentary structures, the joint inversion

362 would simply not converge to a stable solution (Figure S6); even for a 1.0 km thick  
363 sedimentary layer in the starting model, the solution was still not converging (Figure  
364 S7). Assuming a thicker sedimentary layer (i.e., 1.5, 2.0, and 2.5 km), the inversions  
365 yielded more stable solutions (Figures S8–S10). Furthermore, the match between  
366 predicted and observed data, particularly for the P-to-S conversions between 1 and 4 s  
367 (likely corresponding to sedimentary structure) in receiver functions and the Rayleigh  
368 wave dispersions at shorter periods, was superior when we considered a 1.5 km thick  
369 sedimentary layer (Figures S8-S10). Accordingly, we regarded this inverted S-wave  
370 velocity profile (Figure S8) as the final solution for station NEA6.

371         Small misfits in the receiver function waveforms (Figures 3, 4) remain  
372 nonetheless after modelling all the averages and dispersion curve with a single velocity-  
373 depth profile. These small discrepancies, probably indicative of localized lateral  
374 variations in Earth structure, allow us to assess the uncertainties of 1-D inverted shear-  
375 wave velocity models (e.g., Julià et al., 2009). At a given station, we achieved single-  
376 group S-wave velocity models by jointly inverting the dispersion curve with each  
377 individual receiver function average (both high- and low-frequency). The standard  
378 deviations of these single-group models were considered as the approximate  
379 uncertainties (i.e., confidence bounds) for the average velocity model. The above steps  
380 were carried for all stations and the uncertainties were displayed around the average 1-  
381 D velocity-depth profiles (Figures 3, 4). Note that the accuracy of the confidence  
382 bounds is affected by the number of receiver function groups and the regularization  
383 parameters for each station. Nevertheless, we think this approach successfully conveys  
384 the degree of lateral variation around the station and provides a good approximation of  
385 the range of variation in S-velocity.

## 386 **4. Crustal and Upper-Mantle Structure of Northeast China**

387           With the 225 irregularly distributed 1-D velocity profiles, we generated a 3-D  
388 shear-wave velocity model of the crust and upper mantle in Northeast China by  
389 applying a bilinear interpolation for each depth layer. For those stations where we  
390 imposed a thin, near-surface layer to model sedimentary structure, the Voigt average of  
391 the top 2.5-km was calculated to ensure a consistent format. In this section, we present  
392 horizontal and vertical slices of our final 3-D model across the entire study area.

### 393 **4.1. Horizontal slices of Shear-Wave Velocity**

394           Figures 5-7 display a series of horizontal absolute S-velocity maps at different  
395 depths. At shallow levels (i.e., 0–5.0 km, Figure 5a, b), the velocity patterns are  
396 dominated by the presence or absence of sediments. The slow velocities correlate well  
397 with the thick sedimentary cover of the SLB, Sanjiang, Hailar and Erlian basins,  
398 consistent with previous investigations (e.g., Feng et al., 2010; Liu et al., 2016; Guo et  
399 al., 2016). Particularly, the border outlining the low velocities in the center of the study  
400 area closely coincides with the geological boundary of the SLB. At 7.5-15 km depth  
401 (Figure 5d-f), the velocity distributions appear reversed with respect to the shallower  
402 maps. The SLB is characterized by S-wave velocities that are faster (~3.6-3.9 km/s)  
403 than the surrounding areas (~3.2-3.6 km/s). Between 15 km and 25 km depth (Figure  
404 5g, h, and Figure 6a, b), the shear-wave velocities fluctuate around a mean crustal  
405 velocity of ~3.6 km/s, although moderately slow velocities are imaged below the LXM  
406 (around the Wudalianchi volcano) and the northern margin of the North China craton.

407           At crust-to-mantle transition levels (i.e., 27.5–37.5 km, Figure 6d-g), a fast/slow  
408 S-velocity split across the GXM is imaged. As shown later, this pattern results from  
409 changes in crustal thickness, so that velocities West and East of the GXM correspond

410 to mapping the lower crust and uppermost mantle beneath the region, respectively. At  
411 37.5-40 km (Figure 6h), most of the study area displays shear velocities higher than 4.3  
412 km/s - except some local regions in the West at roughly 117°E longitude -  
413 demonstrating that upper mantle levels have been reached beneath Northeast China.

414 At shallow mantle levels (i.e., 40-65 km, Figure 6i-l, and Figure 7a-c), the  
415 reversed velocity pattern imaged at upper-crustal depths (i.e., 7.5-15 km, Figure 5d-f)  
416 seems to reappear. The SLB in the center exhibits high-to-moderate S-velocities, while  
417 low velocities mainly concentrate on the surrounding areas. In the deeper mantle (i.e.,  
418 70-125 km, Figure 7d-i), a reversed fast/slow S-velocity split pattern is revealed. At 70-  
419 75 km depth, the east (i.e., the CBM, Sanjing basin) is characterized by lower S-  
420 velocities, while the west shows high velocities. As depth increases, low velocity zones  
421 expand westward.

## 422 **4.2. Map of Crustal Thickness**

423 To illuminate the contrast in crustal thickness across the entire study area, we  
424 constructed a map of crustal thickness based on the inverted S-velocity models.  
425 Velocities above 4.2 km/s are interpreted as indicative of (hot) uppermost mantle  
426 lithologies. With this simple criterion, we first extracted a crustal thickness estimate  
427 below each station and then constructed a 2-D map through a bilinear interpolation.

428 Figure 8 compares the resulting map of crustal thickness with that from the  
429 global reference model CRUST1.0 (Laske et al., 2013). In general, the two maps exhibit  
430 similarities in large-scale features such as a relatively thicker crust in the west (i.e., the  
431 GXM and its western flank) and a thinner crust in the east (including the CBM, LXM,  
432 SLB, and Sanjiang basin). However, our high-resolution results indicate several  
433 detailed features that differ significantly from the reference model. For example, our

434 model reports a thinner crust of ~30 km in the easternmost portions of the SLB and  
435 LXM, although the locations of minimum crustal thickness for each map coincide.  
436 Additionally, our results reveal a thick crust of more than 40 km west of ~117°E, but  
437 not under the GXM as inferred by CRUST1.0.

438         The most intriguing feature resolved by our model, however, is the abrupt  
439 change in crustal thickness between the Songliao block and Jiamusi massif on either  
440 side of the Mudanjiang fault. Previous studies (Oh, 2006; Wu et al., 2011) claimed that  
441 the Jiamusi massif is possibly an exotic terrane from the Yangtze plate or the  
442 Gondwanan crust. Zhou & Wilde (2013) proposed the Jiamusi massif split away at  
443 ~230 Ma, and subsequently re-docked with the Songliao block between 210 and 180  
444 Ma. Our results demonstrate the difference in crustal thickness between the two blocks.

#### 445 **4.3. Vertical Slices of Shear-Wave Velocity**

446         Vertical sections of S-velocity are plotted in Figures 9-11 for crustal levels (0-  
447 50 km), and in Figures 12-14 for upper-mantle levels (25-125 km). Profiles A1 to A4  
448 are oriented in a west-east direction along latitudes of 48°N, 46°N, 44°N, and 42°N,  
449 respectively. Cross sections B1 to B3 are along longitudes of 120°E, 124°E, and 128°E  
450 in a south-north orientation. Transects C1 to C3 are trending NW-SE.

451         The vertical slices reveal detailed structural information at crustal and upper-  
452 mantle depths. In the crust, we observe four main features: (1) a low shear velocity belt  
453 at 7.5-12.5 km depth below Northeast China except the SLB (Figures 9-11), (2) a very  
454 fast S-velocity body at 8-30 km depth under the SLB (see sections A1, A2, A3 in Figure  
455 9, B2 in Figure 10, and C2 in Figure 11), (3) high S-velocities between 15 and 35 km  
456 depth beneath the CBM region (see profiles A2, A3, A4 in Figure 9, B3 in Figure 10,  
457 and C1, C2 in Figure 11), and (4) some high velocity anomalies at 10-25 km in the west

458 (profiles A2, A3 in Figure 9, and C3 in Figure 11).

459 In the upper mantle, the most intriguing features are the multi-scale, low shear-  
460 wave velocity anomalies below the CBM (see cross sections A3, A4 in Figure 12, B3  
461 in Figure 13, and C2 in Figure 14) and LXM (see A1 in Figure 12, B3 in Figure 13, and  
462 C1 in Figure 14). An additional low velocity zone at 40-60 km depth is revealed beneath  
463 the LXM. A few small-scale low S-velocity anomalies are also imaged at shallow levels  
464 (i.e., 40-60 km, Figures 12-14), implying a more complex system in Northeast China.  
465 In addition, a remarkable high velocity anomaly under the SLB at roughly 50-90 km  
466 depth (see profiles A2 in Figure 12, B2 in Figure 13, and C2 in Figure 14) is observed.

467 A decrease in shear-wave velocity below 4.3 km/s is interpreted as  
468 representative of the lithosphere-asthenosphere boundary (LAB). Our model infers a  
469 very thin lithosphere of 50-70 km thick under the CBM, and a lithospheric thickening  
470 westward (A3, A4 in Figure 12, and C2, C3 in Figure 14). Both the SLB and LXM have  
471 a roughly 100 km thick lithosphere (A1, A3 in Figure 12, B3 in Figure 13, and C1, C2  
472 in Figure 14). The lithospheric thickness under the SLB in our model disagrees with  
473 the recent surface wave tomography of Guo et al. (2016) (they reported high S-  
474 velocities at 50-200 km depths below the SLB), but is consistent with the previous  
475 geophysical studies (e.g., Li et al., 2012; Zhang et al., 2014). Furthermore, we do not  
476 observe the LAB within our depth-range (i.e., 0-125 km) beneath the GXM and its  
477 western flank. This suggests a thicker lithosphere, in agreement with previous studies  
478 (e.g., Zhang et al., 2014).

## 479 **5. Discussion and Implications**

480 The most prominent signatures from our 3-D model are the multi-scale shear-  
481 wave velocity anomalies at different depths in the study area. In the following, we first

482 discuss possible factors that may be responsible for the observed S-velocity anomalies  
483 in the crust and upper mantle. Then, we compare the lithospheric S-velocity structure  
484 of Northeast China and the SLB with the Precambrian lithospheres of the Arabian shield  
485 and North American craton as well as the lithosphere of the Basin and Range in Western  
486 United States, respectively.

### 487 **5.1. Crustal Shear Velocity Anomalies**

488 We image a low S-velocity belt at roughly 7.5-12.5 km depth. Interestingly, the  
489 belt covers the entire Northeast China region except the SLB in its center (Figure 5d,  
490 e). This pattern coincides with the widespread distribution of Cenozoic volcanism in  
491 the region, which is absent in the SLB. Thus, the existence of the low S-velocity belt at  
492 upper-crustal depths appears to be associated with Cenozoic volcanism/magmatism in  
493 Northeast China.

494 Several factors could be involved in the reduction of crustal S-velocity, such as  
495 temperature increase, presence of partial melt, and fluid-filled faults (Tang et al., 2019;  
496 Wang et al., 2019). Considering that surface heat-flow varies between 40 and 105  
497  $mWm^2$  in Northeast China (Gosnold, 2011), it seems plausible to assume a warmer-  
498 than-average crust for Northeast China. Absolute S-wave velocities within the belt are  
499 roughly between 3.2 and 3.4 km/s in our model, so S-velocity reductions are  
500 approximately 0.06-0.26 km/s (equivalent to 1.7-7.5%) relative to the AK135 reference  
501 model (the upper-crustal shear velocity is 3.46 km/s). A temperature increase in the  
502 wide 170-740 °C range may explain the observed velocity reductions through the  
503 scaling relationship  $\partial V_s/\partial T = 0.35 ms^{-1}K^{-1}$  (Sumino & Anderson, 1982).  
504 Temperatures at 10 km depth are usually within the 120-300 °C range for the given  
505 surface heat-flow (Christensen & Mooney, 1995), so such a large temperature increase

506 seems unlikely at this depth. Therefore, although temperature is possibly contributing,  
507 it may not be the only cause for the observed upper-crustal low velocity belt.

508         Ascending magmas may stall within the crust and lead to strong fractional  
509 crystallization (Fan et al., 1999, 2005). Local geophysical studies (e.g., Hammond et  
510 al., 2019; Gao et al., 2020; Kyong-Song et al., 2016; Li et al., 2016; Tang et al., 2001;  
511 Zhang et al., 2002) reported evidence of crustal partial melts and/or magma reservoirs  
512 under the Wudalianchi and Changbaishan volcanic fields. Additionally, deep magmas  
513 were transported upward through the crust via the development and propagation of  
514 faults (Downs et al., 2018). Meanwhile, some liquid and/or gas could have migrated  
515 into these faults, changing the physical properties of the nearby rock. Thus, partial melt  
516 and fluid-filled faults are also likely significant causes for producing the crustal low S-  
517 velocity belt below active magmatic provinces.

518         Our model resolves three significant crustal high velocity features. The most  
519 remarkable one is the extremely fast S-velocity body at 8-30 km below the SLB, which  
520 corroborates previous findings (Guo et al., 2015), but is imaged here with improved  
521 spatial resolution. The very large S-velocity anomaly in the crust was interpreted as  
522 solidified mafic intrusions, consistent with the scenario of widespread  
523 volcanism/magmatism in the region, followed by cooling and subsidence during the  
524 late Mesozoic under the SLB (Feng et al., 2010).

525         Beneath the active Cenozoic magmatic province - CBM, high S-velocities at 15-  
526 35 km depths are observed in our model. This observation differs from the recent  
527 surface wave tomographic study of Fan et al. (2020), in which they reported a slow S-  
528 velocity anomaly attributed to a potential lower-crustal magma reservoir below the  
529 CBM. We interpret the observed fast S-velocity underneath the CBM as the result of

530 middle to lower-crustal magmatic intrusions (through cooling and solidification).

531 Like the SLB, the GXM also experienced extensive volcanism/magmatism  
532 possibly caused by delamination and consequent asthenospheric mantle upwelling  
533 during the late Mesozoic (Wang et al., 2006; Wu et al., 2005; Zhang et al., 2010). Thus,  
534 we observe crustal high S-velocity anomalies (at 10-25 km depth) that probably reflect  
535 magmatic intrusions, although the size of the fast S-velocity anomalies under the GXM  
536 and its western flank is not comparable to that of the one below the SLB. Geochemical  
537 studies (e.g., Zhang et al., 2010) reported granite emplacement in Mesozoic volcanic  
538 rocks in the GXM. This finding may explain why felsic crust is predominant under this  
539 subregion (Guo et al., 2016).

540 Interestingly, below the LXM (around the Wudalianchi volcano), no fast S-  
541 velocity anomaly is observed at crustal depths, which is obviously different from the  
542 other active Cenozoic magmatic provinces such as the CBM. The LXM shows a lower  
543 crust with moderately slow shear velocities. Recent local investigations (Gao et al.,  
544 2020; Li et al., 2016) imaged an extremely low-resistivity and low-velocity body,  
545 interpreted as a magma chamber, at upper-crustal levels below one vent of the  
546 Wudalianchi volcano. Accordingly, the observed moderately low S-velocity in the  
547 lower crust may be associated with upward transportation of magmas and charging of  
548 the crustal reservoir from deep mantle sources.

## 549 **5.2. Upper-Mantle Shear Velocity Anomalies**

550 Our model confirms the existence of a pronounced upper-mantle low shear  
551 velocity zone beneath the CBM, which is consistent with previous studies (e.g., Guo et  
552 al., 2016; Li et al., 2012; Pan et al., 2015; Tang et al., 2014; Zhao et al., 2009). Our  
553 model resolves new details about the low velocity zone including its geometry and

554 minimum absolute velocity. S-wave velocities less than 4.25 km/s can be regarded as  
555 representative of partial melts in the upper mantle, particularly beneath volcanically  
556 active fields (Plank & Forsyth, 2016). Therefore, the observed low velocity zone ( $V_s <$   
557 4.25 km/s) strongly suggests the presence of partial melts in the upper mantle.

558 Previous studies proposed hot and wet upwelling flows in a big mantle wedge  
559 (Zhao et al., 2004, 2009) or an upward escape of melted sub-slab materials through the  
560 stagnant Pacific slab gap in the mantle transition zone (Tang et al., 2014), which  
561 triggered the volcanism. While the deep mantle dynamics are still debated, there is  
562 widespread agreement that the upwelling of hot sub-lithospheric melts feed the  
563 volcanism in the CBM. A mantle anisotropy study of Li et al. (2017) with SKS data  
564 reported extensive null splitting in the CBM, likely consistent with the upwelling  
565 model. Thus, the imaged upper-mantle low velocity zone most likely reflects a large  
566 volume of upwelling mantle melts.

567 Some studies (e.g., Wei et al., 2019; Zhao et al., 2009) speculated that the  
568 Cenozoic volcanism in the LXM (e.g., Wudalianchi volcano) has the same origin as the  
569 volcanoes in the CBM: triggered by upward flows of hot mantle materials. Below the  
570 LXM, we image a pronounced upper-mantle low velocity zone ( $V_s < 4.25$  km/s, below  
571  $\sim 100$  km) that can be interpreted as upwelling asthenospheric mantle melt, consistent  
572 with the dynamic model of Zhao et al. (2009). However, our results exhibit an  
573 additional low S-velocity anomaly in the uppermost mantle ( $V_s < 4.25$  km/s, at 40-60  
574 km depth), probably representing partial melts also beneath the LXM. The distinctions  
575 between the LXM and CBM in lithospheric structure include: (1) moderately slow S-  
576 velocity under the LXM versus high S-velocity below the CBM in the lower crust, (2)  
577 a 30 km thick crust under the LXM versus a roughly 35 km thick crust under the CBM,

578 (3) a ~100 km thick continental lithosphere containing an uppermost-mantle low S-  
579 velocity anomaly at 40-60 km beneath the LXM versus thinner lithosphere (50-70 km)  
580 under the CBM, which may be associated with the differences in volcanic/magmatic  
581 activity and basalt geochemistry in the two provinces (Fan et al., 2021).

582         The SLB is the center of the late Mesozoic rifting and lithospheric thinning in  
583 eastern China (Ren et al., 2002). Our model displays a thin lithosphere (~100 km) below  
584 the SLB, consistent with the episode of the intensive extension (Feng et al., 2010; Ren  
585 et al., 2002). However, an interesting phenomenon is the absence of Cenozoic  
586 volcanism in the SLB. Invoking the model of wet, hot upwelling caused by dehydration  
587 of the stagnant Pacific slab in the mantle transition zone (Zhao et al., 2009, 2012) raises  
588 a problem: why did volcanism not occur in the SLB during the Cenozoic, as it did in  
589 the western interior (e.g., Halaha and Abaga volcanoes)? One possible explanation is  
590 that the extensive volcanic/magmatic activities during the late-Mesozoic depleted the  
591 lithosphere under the SLB and made it more refractory. Thus, the lithosphere of the  
592 SLB could not produce any melts for Cenozoic volcanism. One evidence - a positive  
593 mantle velocity anomaly under the SLB (at 50-90 km depth) revealed by our model can  
594 support this hypothesis.

595         Another possibility is invoking the mantle convection model raised by Guo et  
596 al. (2016). They proposed the mantle upwelling below the CBM led to a downwelling  
597 asthenospheric flow under the SLB. If the hypothetical mantle convection exists, the  
598 hot sub-lithospheric melts beneath the SLB would lack the driving force to migrate  
599 upward and would not induce volcanism. Mantle anisotropy studies (Chen et al., 2017;  
600 Li et al., 2017) exhibited many nulls in the CBM, a few nulls in the southwestern SLB,  
601 and some nearly NW-SE fast polarization directions in between from shear wave

602 splitting measurements. The nulls in the southwestern SLB are attributed to the  
603 downwelling limb of the convection cell (Li et al., 2017).

604 A simple asthenospheric mantle flow usually cannot explain the observed  
605 seismic anisotropy, which also reflects historical tectonic deformation preserved in the  
606 lithosphere (Li & Niu, 2010; Liu et al., 2016; Qiang & Wu, 2015). In the SLB, weak  
607 azimuthal anisotropy approximately corresponding to crustal and lithospheric mantle  
608 depths suggests that historical deformation records in the lithosphere were erased by  
609 the extensive volcanism/magmatism in the late Mesozoic (Liu et al., 2016).  
610 Accordingly, we could consider the asthenospheric mantle flow as the dominant factor  
611 determining the mantle anisotropy of the SLB.

612 However, only a few stations show nulls. Moreover, complicated variations of  
613 shear wave splitting within the SLB were observed (Chen et al., 2017; Li et al., 2017).  
614 Thus, there is still insufficient evidence to support a downwelling flow in the SLB due  
615 to mantle convection. Besides, a high P-wave velocity anomaly resting atop the 410 km  
616 discontinuity under the SLB was imaged and interpreted as detached continental  
617 lithosphere by Wei et al. (2019). If their imaging and interpretation are correct, the  
618 continuous sinking of the delaminated lithosphere could induce an upward flow, in  
619 conflict with the mantle convection model.

### 620 **5.3. Comparison with Other Lithospheric Models**

621 For comparison, we average the 225 1-D shear-wave velocity models obtained  
622 from the joint inversion at each station to generate a single 1-D average model for  
623 Northeast China. Also, we average all the 1-D S-velocity models from the stations  
624 located in the SLB to obtain one average 1-D model that represents the extended  
625 lithosphere of the SLB. Figure 16a compares the S-velocity structure of Northeast

626 China with the Precambrian lithospheres of the Arabian shield (Tang et al., 2019) and  
627 the North American craton (Shen & Ritzwoller, 2016). Additionally, Figure 16b  
628 exhibits the comparison between the rift lithosphere of the SLB in Northeast China and  
629 that of the Basin and Range (Shen & Ritzwoller, 2016) in Western United States.

630         Generally, the Precambrian crusts of different regions appear similar (Figure  
631 15a). Both the Arabian shield and Northeast China have a thinner crust of ~35 km,  
632 compared with the North American craton (~45 km thick crust). That is probably  
633 because the former two experienced intensive rifting (Ebinger & Sleep, 1998; Ren et  
634 al., 2002). Above all, one significant observation from the 1-D average model of  
635 Northeast China is the constant  $V_s$  (~3.6 km/s) between 15 and 27.5 km, distinctly  
636 different from the Arabian shield and the North American craton. What could be the  
637 major factor to induce a near-zero seismic velocity gradient within the depth levels?  
638 We attribute it to temperature and conclude that the crust of Northeast China is likely  
639 rather warm, although other potential factors such as crustal partial melts within some  
640 local areas may also contribute.

641         The reductions in S-velocity at 15–27.5 km depths below Northeast China are  
642 approximately 0.1-0.2 km/s, compared with the Arabian shield and the North American  
643 craton. The corresponding crustal temperature increases are 280-570 °C, simply  
644 estimated with the relationship  $\partial V_s / \partial T = 0.35 \text{ ms}^{-1} \text{ K}^{-1}$  (Sumino & Anderson, 1982).  
645 Considering the temperature-depth models for Eastern United States (200-400 °C  
646 between 15 and 27.5 km for average heat flow, Blackwell, 1971; Christensen &  
647 Mooney, 1995), however, temperatures within 15–27.5 km depth in Northeast China  
648 are probably larger, around 480-970 °C (consistent with high heat flow).

649         Furthermore, for Northeast China, the S-velocity of the uppermost mantle is

650 approximately 4.35 km/s, which is ~0.1 km/s lower than the Arabian shield and North  
651 American craton. This characteristic probably suggests a slightly warm uppermost  
652 mantle. Temperature anomalies at both the crust and uppermost mantle are likely  
653 associated with the active intraplate volcanism in Northeast China.

654 Using the first-order Taylor expansion of the pressure-temperature dependence  
655 of the shear wave velocity,  $V_s(P, T) = V_0(P_0, T_0) + \frac{\partial V_s}{\partial P}(P - P_0) + \frac{\partial V_s}{\partial T}(T - T_0)$ , we  
656 simply estimate the average temperature of the uppermost mantle in Northeast China.  
657 This expression relates  $V_s$  at a given pressure  $P$  and temperature  $T$  with a reference  
658 velocity  $V_0$  at pressure  $P_0$  and temperature  $T_0$  through the partial derivatives  $\partial V_s/\partial P$   
659 and  $\partial V_s/\partial T$ . Assuming that the dominant rock within the uppermost mantle is  
660 peridotite, the estimates for the reference velocity  $V_0 = 4.72 \text{ km/s}$  (at pressure  $P_0 =$   
661  $0 \text{ kbar}$  and temperature  $T_0 = 0 \text{ }^\circ\text{C}$ ) and the partial derivatives ( $\partial V_s/\partial P = 0.946 \times$   
662  $10^{-2} \text{ km/s}\cdot\text{kbar}$  and  $\partial V_s/\partial T = -3.93 \times 10^{-4} \text{ km/s}\cdot^\circ\text{C}$ ) are taken from Kern & Richter  
663 (1981). Pressure is estimated as  $P = \sum_i \rho_i g h_i$ , where  $i$  is the layer number,  $\rho_i$   
664 represents the density at  $i$ th layer from the average 1-D model,  $g$  is gravity acceleration,  
665 and  $h_i$  represents the thickness of  $i$ th layer. For the average S-velocity (~4.35 km/s) of  
666 the uppermost mantle (at 40 km depth), the estimated temperature is ~1200 °C.

667 For comparison between the SLB and the Basin and Range (Figure 15b), we  
668 note that the SLB has a pronounced fast S-velocity anomaly at 7.5-17.5 km depth,  
669 which is interpreted as solidified mafic magmatic intrusions during the late Mesozoic.  
670 Additionally, the S-velocity of the uppermost mantle in the Basin and Range is about  
671 4.2 km/s, much lower than that (~4.4 km/s) of the SLB. The Basin and Range has a  
672 significantly warm upper mantle (Blackwell, 1971; Christensen & Mooney, 1995).  
673 Thus, this implies the Basin and Range is much warmer than the SLB, which is

674 moderately warm. With the same approach introduced above, the estimated average  
675 temperature of the uppermost mantle (at 40 km depth) of the SLB is ~1080 °C.

## 676 **6. Conclusions**

677 We have constructed a high-resolution 3-D S-wave velocity model of the crust  
678 and upper mantle for Northeast China by jointly inverting receiver functions and  
679 fundamental-mode Rayleigh wave group velocities for 225 broadband seismic stations.  
680 Our results reveal the detailed lithospheric and sub-lithospheric structure, and shed light  
681 on the volcanic/magmatic processes and dynamics (Figure 16). Our main findings and  
682 interpretations associated with the shear velocity structure in Northeast China are  
683 shown in Figure 16 and summarized as follows:

- 684 1. We observe a low S-velocity belt at 7.5-12.5 km depth, which covers entire  
685 Northeast China except the SLB in the center. We conjecture that the slow  
686 S-velocity belt may be associated with Cenozoic volcanism in Northeast  
687 China and is likely the result of multiple factors including a temperature  
688 anomaly, partial melts, and fluid-filled faults.
- 689 2. Our model resolves localized fast S-velocity anomalies in the crust.  
690 Particularly, the positive S-velocity anomaly below the SLB is interpreted  
691 as late-Mesozoic mafic intrusions. The high S-velocity under the CBM is  
692 attributed to middle to lower-crustal solidified magmatic intrusions.
- 693 3. Our model confirms the upper-mantle low shear velocity zones below the  
694 CBM and LXM, which support the geodynamic model of sub-lithospheric  
695 mantle melt upwellings. Additionally, our results reveal significant  
696 distinctions in lithospheric structure between the LXM and CBM, which  
697 may be associated with the differences in volcanic/magmatic activity and

698 basalt geochemistry in the two subregions.

699 4. A positive mantle S-velocity anomaly at 50-90 km depth beneath the SLB  
700 is imaged, which may reflect a depleted and more refractory lithosphere  
701 resulted from the extensive late-Mesozoic volcanism/magmatism and thus  
702 explain the absence of Cenozoic volcanism in the SLB.

703 5. The lithosphere-asthenosphere boundary (LAB) is evidenced by a decrease  
704 in S-wave velocity below 4.3 km/s. The LAB depth increases systematically  
705 from east to west in our study area. The LAB depth is 50-70 km beneath the  
706 CBM, 100 km beneath the SLB, and exceeds 125 km beneath the GXM.

707 6. In comparison with the Arabian shield and North American craton, the crust  
708 underneath Northeast China is likely rather warm (~480-970 °C between 15  
709 and 27.5 km depth), as it is the uppermost mantle (~1200 °C), and probably  
710 associated with the active intraplate volcanism. The SLB, nonetheless,  
711 possesses a moderately warm uppermost mantle (~1080 °C).

## 712 **Acknowledgements**

713 We are grateful to the NECESSArray Project Team for sharing the waveform  
714 data of the portable seismic stations, which were downloaded from Incorporated  
715 Research Institutions for Seismology (IRIS). The teleseismic waveform data recorded  
716 by the permanent stations were provided by China Seismic Data Management Center  
717 at Institute of Geophysics, China Earthquake Administration, and can be accessed from  
718 the data center (<http://www.chinarraydmc.cn>). We sincerely thank Jessica Reid for her  
719 constructive comments that greatly help to improve the manuscript. The research  
720 presented in the paper is supported by the National Science Foundation of China (grant  
721 41974011) and MOST grant (2018YFC1503606) in China. J.J. thanks the Conselho

722 Nacional de Desenvolvimento Científico e Tecnológico (CNPq) for his continued  
723 research fellowship (CNPq 308644/2019-0). P.M.M. is supported by funding from  
724 King Abdullah University of Science and Technology, grant number BAS/1/1339-01-  
725 01.

## 726 **References**

727 Ammon, C. J., Randall, G. E., & Zandt, G. (1990). On the nonuniqueness of receiver  
728 function inversions. *Journal of Geophysical Research: Solid Earth (1978–*  
729 *2012)*, 95(B10), 15303-15318.

730 Berteussen, K. A. (1977). Moho depth determinations based on spectral-ratio analysis  
731 of NORSAR long-period P waves. *Physics of the Earth and Planetary Interiors*,  
732 15(1), 13-27.

733 Blackwell, D. D. (1971). The thermal structure of the continental crust, in *The*  
734 *Structure and Physical Properties of the Earth's Crust, Geophys. Monogr. Ser.*,  
735 vol. 14, edited by J. G. Heacock, pp. 169-184, AGU, Washington, D.C., 1971.

736 Chen, H., Niu, F., Obayashi, M., Grand, S. P., Kawakatsu, H., Chen, Y. J., Ning, J., &  
737 Tanaka, S. (2017). Mantle seismic anisotropy beneath NE China and  
738 implications for the lithospheric delamination hypothesis beneath the southern  
739 Great Xing'an range. *Earth and Planetary Science Letters*, 471, 32–41.

740 Chen, Y., Zhang, Y., Graham, D., Su, S., & Deng, J. (2007). Geochemistry of  
741 Cenozoic basalts and mantle xenoliths in Northeast China. *Lithos*, 96(1-2),  
742 108–126.

743 ChinaNetwork. (2006). China Seismic Network waveform data. China Earthquake  
744 Administration, doi:10.12001/ChinaNetwork.Data.

745 Christensen, N. I., & Mooney, W. D. (1995). Seismic velocity structure and  
746 composition of the continental crust: A global view. *Journal of Geophysical*  
747 *Research: Solid Earth*, 100(B6), 9761-9788.

748 Deng, J., Zhao, H., Mo, X., Luo, Z., & Du, S. (1996). Continental root/plume structure  
749 in China—Key to the continental geodynamics (pp. 1–110). *Beijing: Geological*

750 *Publishing House.*

751 Downs, D. T., Stelten, M. E., Champion, D. E., Dietterich, H. R., Nawab, Z., Zahran,  
752 H., ... & Shawali, J. (2018). Volcanic history of the northernmost part of the  
753 Harrat Rahat volcanic field, Saudi Arabia. *Geosphere*, 14(3), 1253-1282.

754 Dziewonski, A. M., & Anderson, D. L. (1981). Preliminary reference Earth model.  
755 *Physics of the earth and planetary interiors*, 25(4), 297-356.

756 Ebinger, C. J., & Sleep, N. H. (1998). Cenozoic magmatism throughout east Africa  
757 resulting from impact of a single plume. *Nature*, 395(6704), 788-791.

758 Fan, Q., & Hooper, P. R. (1991). The Cenozoic basaltic rocks of eastern China:  
759 Petrology and chemical composition. *Journal of Petrology*, 32(4), 765–810.

760 Fan, Q., Liu, R., & Li, D. (1999). Significance of K-Ar age of bimodal volcanic rocks  
761 at Wangtian'e volcano, Changbaishan area. *Chinese Sciences Bulletin*, 44(7):  
762 660-663.

763 Fan, Q., Sui, J., Sun, Q., Li, N., & Wang, T. (2005). Preliminary research on magma  
764 mixing and explosive mechanism of the Millennium eruption of Tianchi  
765 volcano (in Chinese with English abstract). *Acta Petrologica Sinica*,  
766 21(6):1703-1708.

767 Fan, X., Chen, Q., Ai, Y., Chen, L., Jiang, M., Wu, Q., & Guo, Z. (2021). Quaternary  
768 sodic and potassic intraplate volcanism in the Northeast China controlled by the  
769 underlying heterogeneous lithospheric structures. *Geology*, 49.

770 Fan, X., Chen, Q., Legendre, C. P., & Guo, Z. (2020). Intraplate volcanism and  
771 regional geodynamics in NE Asia revealed by anisotropic Rayleigh-wave  
772 tomography. *Geophysical Research Letters*, 47.

773 Feng, Z., Jia, C., Xie, X., Zhang, S., Feng, Z., & Cross, T. A. (2010).  
774 Tectonostratigraphic units and stratigraphic sequences of the nonmarine  
775 Songliao basin, northeast China. *Basin Research*, 22, 79–95.

776 Gosnold, W. (2011). The Global Heat Flow Database. The International Heat Flow  
777 Commission: <https://ihfc-iugg.org/products/global-heat-flow-database>.

778 Julià, J. (2007). Constraining velocity and density contrasts across the crust-mantle

779 boundary with receiver function amplitudes. *Geophysical Journal International*,  
780 171(1), 286-301.

781 Julià, J., Ammon, C. J., & Herrmann, R. B. (2003). Lithospheric structure of the  
782 Arabian Shield from the joint inversion of receiver functions and surface-wave  
783 group velocities. *Tectonophysics*, 371(1), 1-21.

784 Julià, J., Ammon, C. J., Herrmann, R. B., & Correig, A. M. (2000). Joint inversion of  
785 receiver function and surface wave dispersion observations. *Geophysical  
786 Journal International*, 143(1), 99-112.

787 Julià, J., Herrmann, R. B., Ammon, C. J., & Akinç, A. (2004). Evaluation of deep  
788 sediment velocity structure in the New Madrid Seismic Zone. *Bulletin of the  
789 Seismological Society of America*, 94, 334–340.

790 Julià, J., Jagadeesh, S., Rai, S. S., & Owens, T. J. (2009). Deep crustal structure of the  
791 Indian shield from joint inversion of P wave receiver functions and Rayleigh  
792 wave group velocities: Implications for Precambrian crustal evolution. *Journal  
793 of Geophysical Research: Solid Earth*, 114, B10313.

794 Hammond, J., Wu, J., Ri, K., Wei, W., Yu, J., & Oppenheimer, C. (2019). Distribution  
795 of partial melt beneath Changbaishan/Paektu volcano, China/Democratic  
796 people's Republic of Korea. *Geochemistry, Geophysics, Geosystems*, 21(1).

797 He, C., Dong, S., Chen, X., Santosh, M., & Niu, S. (2013). Seismic evidence for  
798 plume-induced rifting in the Songliao basin of Northeast China. *Tectonophysics*,  
799 627, 171–181.

800 Huang, J., & Zhao, D. (2006). High-resolution mantle tomography of China and  
801 surrounding regions. *Journal of Geophysical Research*, 111, B09305.

802 Gao, J., Zhang, H., Zhang, S., Xin, H., Li, Z., Tian, W., Bao, F., Cheng, Z., Jia, X., &  
803 Fu, L. (2020). Magma recharging beneath the Weishan volcano of the intraplate  
804 Wudalianchi volcanic field, northeast China, implied from 3-D magnetotelluric  
805 imaging. *Geology*, 48.

806 Ge, X. H., & Ma, W. P. (2007). Mesozoic-Cenozoic tectonic framework of southern  
807 Northeast Asia. *Geology in China*, 34, 212–228.

- 808 Guo, Z., Chen, Y. J., Ning, J., Feng, Y., Grand, S. P., Niu, F., Kawakatsu, H., Tanaka,  
809 S., Obayashi, M., & Ni, J. F. (2015). High resolution 3-D crustal structure  
810 beneath NE China from joint inversion of ambient noise and receiver functions  
811 using NECESSArray data. *Earth and Planetary Science Letters*, *416*, 1–11.
- 812 Guo, Z., Chen, Y. J., Ning, J., Yang, Y., Afonso, J. C., & Tang, Y. (2016). Seismic  
813 evidence of on-going sublithosphere upper mantle convection for intra-plate  
814 volcanism in Northeast China. *Earth and Planetary Science Letters*, *433*, 31–  
815 43.
- 816 Guo, Z., Wang, K., Yang, Y., Tang, Y., Chen, Y. J., & Hung, S.-H. (2018). The origin  
817 and mantle dynamics of quaternary intraplate volcanism in Northeast China  
818 from joint inversion of surface wave and body wave. *Journal of Geophysical  
819 Research: Solid Earth*, *123*.
- 820 Kern, H., & Richter, A. (1981). Temperature derivatives of compressional and shear-  
821 wave velocities in crustal and mantle rocks at 6 kbar confining pressure. *Journal  
822 of Geophysics -Zeitschrift fur Geophysik*, *49*(1), 47–56.
- 823 Kyong-Song, R., Hammond, J. O. S., Chol-Nam, K., Hyok, K., Yong-Gun, Y., Gil-  
824 Jong, P., Chong-Song, R., Oppenheimer, C., Liu, K. W., Iacovino, K., & Kum-  
825 Ran, R. (2016). Evidence for partial melt in the crust beneath Mt. Paektu  
826 (Changbaishan), Democratic People’s Republic of Korea and China. *Science  
827 Advances*, *2*(4), e1501513.
- 828 Langston, C. A. (1979). Structure under Mount Rainier, Washington, inferred from  
829 teleseismic body waves. *Journal of Geophysical Research: Solid Earth (1978–  
830 2012)*, *84*(B9), 4749-4762.
- 831 Laske, G., Masters, G., Ma, Z., & Pasyanos, M. (2013). Update on CRUST1.0 – A 1-  
832 degree Global Model of Earth’s Crust. *EGU General Assembly Conference  
833 Abstract*, *15*, 2658.
- 834 Lei, J., & Zhao, D. (2005). P-wave tomography and origin of the Changbai intraplate  
835 volcano in Northeast Asia. *Tectonophysics*, *397*(3-4), 281–295.
- 836 Li, C., & Van der Hilst, R. D. (2010). Structure of the upper mantle and transition zone

- 837           beneath Southeast Asia from travelttime tomography. *Journal of Geophysical*  
838           *Research*, 115, B07308.
- 839   Li, J., & Niu, F. (2010). Seismic anisotropy and mantle flow beneath northeast China  
840           inferred from regional seismic networks. *Journal of Geophysical Research*, 115,  
841           B12327.
- 842   Li, S., Guo, Z., & Chen, Y. (2017). Complicated 3D mantle flow beneath Northeast  
843           China from shear wave splitting and its implication for the Cenozoic intraplate  
844           volcanism. *Tectonophysics*, 709, 1–8.
- 845   Li, Y., Wu, Q., Pan, J., & Sun, L. (2012). S-wave velocity structure of northeastern  
846           china from joint inversion of Rayleigh wave phase and group velocities.  
847           *Geophysical Journal International*, 190, 105-115.
- 848   Li, Y., Wu, Q., Pan, J., Zhang, F., & Yu, D. (2013). An upper-mantle S-wave velocity  
849           model for East Asia from Rayleigh wave tomography. *Earth and Planetary*  
850           *Science Letters*, 377-378, 367-377.
- 851   Li, Z., Ni, S., Zhang, B., Bao, F., Zhang, S., Deng, Y., & Yuen, D. A. (2016). Shallow  
852           magma chamber under the Wudalianchi Volcanic Field unveiled by seismic  
853           imaging with dense array. *Geophysical Research Letters*, 43, 4954–4961.
- 854   Ligorria, J. P., & Ammon, C. J. (1999). Iterative deconvolution and receiver-function  
855           estimation. *Bulletin of the seismological Society of America*, 89(5), 1395-1400.
- 856   Liu, H., & Niu, F. (2011). Receiver function study of the crustal structure of Northeast  
857           China: Seismic evidence for a mantle upwelling beneath the eastern flank of the  
858           Songliao Basin and the Changbaishan region. *Earthquake Science*, 24: 27-33.
- 859   Liu, J. (1987). Study on geochronology of the Cenozoic volcanic rocks in Northeast  
860           China (in Chinese with English abstract). *Acta Petrologica Sinica*, (4): 21-31.
- 861   Liu, J., Han, J., & Fyfe, W. S. (2001). Cenozoic episodic volcanism and continental  
862           rifting in northeast China and possible link to Japan Sea development as  
863           revealed from K-Ar geochronology. *Tectonophysics*, 339(3-4), 385–401.
- 864   Liu, Z., Huang, J., & Yao, H. (2016). Anisotropic Rayleigh wave tomography of  
865           Northeast China using ambient seismic noise. *Physics of the Earth and*

- 866 *Planetary Interiors*, 256, 37-48.
- 867 Ma, J., Tian, Y., Liu, C., Zhao, D., Feng, X., & Zhu, H. (2018). P-wave tomography  
868 of Northeast Asia: Constraints on the western Pacific plate subduction and  
869 mantle dynamics. *Physics of the Earth and Planetary Interiors*, 274, 105–126.
- 870 Meng, Q. (2003). What drove late Mesozoic extension of the northern China -  
871 Mongolia tract? *Tectonophysics*, 369(3-4), 155–174.
- 872 Oh, C. W. (2006). A new concept on tectonic correlation between Korea, China and  
873 Japan: histories from the late Proterozoic to Cretaceous. *Gondwana Research*,  
874 9, 47–61.
- 875 Ohtani, E., Litasov, K., Hosoya, T., Kubo, T., & Kondo, T. (2004). Water transport  
876 into the deep mantle and formation of a hydrous transition zone. *Physics of the*  
877 *Earth and Planetary Interiors*, 143, 255–269.
- 878 Owens, T. J., Zandt, G., & Taylor, S. R. (1984). Seismic evidence for an ancient rift  
879 beneath the Cumberland Plateau, Tennessee: A detailed analysis of broadband  
880 teleseismic P waveforms. *Journal of Geophysical Research: Solid Earth (1978–*  
881 *2012)*, 89(B9), 7783-7795.
- 882 Pan, J., Wu, Q., Li, Y., & Yu, D. (2014). Ambient noise tomography in northeast China  
883 (in Chinese with English abstract). *Chinese Journal of Geophysics*, 57: 812-821.
- 884 Pan, J., Li, Y., Wu, Q., & Yu, D. (2015). 3-D S-wave velocity structure of crust and  
885 upper-mantle beneath the northeast China (in Chinese with English abstract).  
886 *Chinese Journal of Geophysics*, 57(7): 2077-2087.
- 887 Plank, T., & Forsyth, D. W. (2016). Thermal structure and melting conditions in the  
888 mantle beneath the Basin and Range province from seismology and petrology.  
889 *Geochemistry, Geophysics, Geosystems*, 17, 1312–1338.
- 890 Qiang, Z., & Wu, Q. (2015). Upper mantle anisotropy beneath the north of northeast  
891 China and its dynamic significance (in Chinese with English abstract). *Chinese*  
892 *Journal of Geophysics*, 58, 3540–3552.
- 893 Ren, J., Tamaki, K., Li, S., & Junxia, Z. (2002). Late Mesozoic and Cenozoic rifting

894 and its dynamic setting in Eastern China and adjacent areas. *Tectonophysics*,  
895 *344*, 175–205.

896 Savage, M. K. (1998). Lower crustal anisotropy or dipping boundaries? Effects on  
897 receiver functions and a case study in New Zealand. *Journal of Geophysical*  
898 *Research: Solid Earth*, *103*(B7), 15069-15087.

899 Şengör, A. M. C., Natalin, B. A., & Burtman, V. S. (1993). Evolution of the Altaid  
900 tectonic collage and Palaeozoic crustal growth in Eurasia. *Nature*, *364*(6435):  
901 299-307.

902 Shen, W., & Ritzwoller, M. H. (2016). Crustal and uppermost mantle structure beneath  
903 the United States. *Journal of Geophysical Research: Solid Earth*, *121*.

904 Sumino, Y., & Anderson, O.L. (1982). Elastic constants in minerals. In: Carmichael,  
905 R.S. (Ed.), *CRC Handbook of Physical Properties of Rocks*. *CRC Press, Boca*  
906 *Raton, FL*, pp. 39–138.

907 Tang, J., Deng, Q., Zhao, G., Bai, D., Jin, G., Li, W., Xuan, F., Zhan, Y., Li, G., Hong,  
908 F., & Ma, M. (2001). Electric conductivity and magma chamber at the Tianchi  
909 volcano area in Changbaishan Mountain, *Seismology and Geology*, *23*, 191–  
910 200.

911 Tang, Y., Obayashi, M., Niu, F., Grand, S. P., Chen, Y. J., Kawakatsu, H., Tanaka, S.,  
912 Ning, J., & Ni, J. F. (2014). Changbaishan volcanism in northeast China linked  
913 to subduction-induced mantle upwelling. *Nature Geoscience*, *7*(6), 470–475.

914 Tang, Z., Julià, J., Zahran, H., & Mai, P. M. (2016). The lithospheric shear-wave  
915 velocity structure of Saudi Arabia: Young volcanism in an old shield.  
916 *Tectonophysics*, *680*, 8-27.

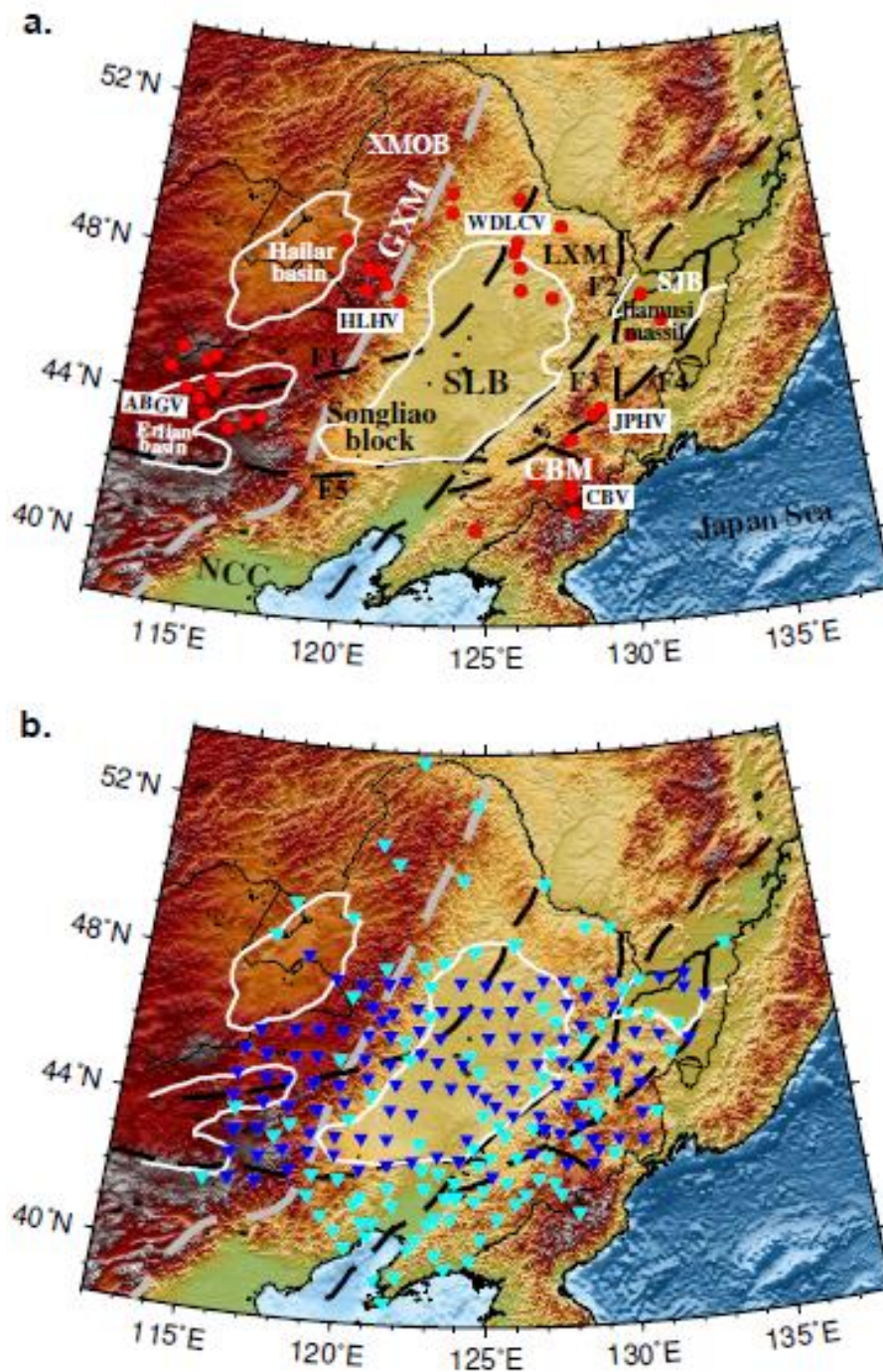
917 Tang, Z., Mai, P. M., Julià, J., & Zahran, H. (2019). Shear velocity structure beneath  
918 Saudi Arabia from the joint inversion of P and S wave receiver functions, and  
919 Rayleigh wave group-velocity dispersion data. *Journal of Geophysical*  
920 *Research: Solid Earth*, *124*.

921 Tao, K., Niu, F., Ning, J., Chen, Y. J., Grand, S., Kawakatsu, H., Tanaka, S., Obayashi,  
922 M., & Ni, J. (2014). Crustal structure beneath NE China imaged by  
923 NECESSArray receiver function data. *Earth and Planetary Science Letters*,

- 924 398, 48–57.
- 925 Tao, K., Grand, S. P., & Niu, F. (2018). Seismic structure of the upper mantle beneath  
926 eastern Asia from full waveform seismic tomography. *Geochemistry,*  
927 *Geophysics, Geosystems, 19*, 2732–2763.
- 928 Tian, Y., Zhu, H., Zhao, D., Liu, C., Feng, X., Liu, T., & Ma, J. (2016). Mantle  
929 transition zone structure beneath the Changbai volcano: Insight into deep slab  
930 dehydration and hot upwelling near the 410-km discontinuity. *Journal of*  
931 *Geophysical Research: Solid Earth, 121*, 5794–5808.
- 932 Wang, F., Zhou, X., Zhang, L., Ying, J., Zhang, Y., Wu, F., & Zhu, R. (2006). Late  
933 Mesozoic volcanism in the Great Xing'an Range (NE China): Timing and  
934 implications for the dynamic setting of NE Asia. *Earth and Planetary Science*  
935 *Letters, 251*(1-2), 179–198.
- 936 Wang, T., Feng, J., Liu, K. H., & Gao, S. S. (2019). Crustal structure beneath the  
937 Malawi and Luangwa Rift Zones and adjacent areas from ambient noise  
938 tomography. *Gondwana Research, 67*, 187-198.
- 939 Wei, H., Liu, J., & Meng, Q. (2010). Structural and sedimentary evolution of the  
940 southern Songliao Basin, northeast China, and implications for hydrocarbon  
941 prospectivity. *American Association of Petroleum Geologists Bulletin, 94*(4),  
942 533–566.
- 943 Wei, W., Hammond, J. O. S., Zhao, D., Xu, J., Liu, Q., & Gu, Y. (2019). Seismic  
944 evidence for a mantle transition zone origin of the Wudalianchi and Halaha  
945 volcanoes in northeast China. *Geochemistry, Geophysics, Geosystems, 20*, 398–  
946 416.
- 947 Wei, W., Xu, J., Zhao, D., & Shi, Y. (2012). East Asia mantle tomography: New  
948 insight into plate subduction and intraplate volcanism. *Journal of Asian Earth*  
949 *Sciences, 60*, 88–103.
- 950 Wei, W., Zhao, D., Xu, J., Wei, F., & Liu, G. (2015). P and S wave tomography and  
951 anisotropy in Northwest Pacific and East Asia: Constraints on stagnant slab and  
952 intraplate volcanism. *Journal of Geophysical Research: Solid Earth, 120*, 1642–

- 953 1666.
- 954 Wu, F., Jahn, B. M., Wilde, S. A., Lo, C., Yui, T., Lin, Q., Ge, W., & Sun, D. (2003).  
955 Highly fractionated I-type granites in NE China (I): geochronology and  
956 petrogenesis. *Lithos*, 66: 241–273.
- 957 Wu, F., Lin, J., Wilde, S. A., Zhang, X., & Yang, J. (2005). Nature and significance of  
958 the Early Cretaceous giant igneous event in eastern China. *Earth and Planetary  
959 Science Letters*, 233(1-2), 103–119.
- 960 Wu, F., Sun, D., Ge, W., Zhang, Y., Grant, M. L., Wilde, S. A., & Jahn, B. M. (2011).  
961 Geochronology of the Phanerozoic granitoids in northeastern China. *Journal of  
962 Asian Earth Sciences*, 41, 1–30.
- 963 Wu, Q., Zheng, X., Pan, J., Zhang, F., & Zhang, G. (2009). Measurement of  
964 interstation phase velocity by wavelet transformation, *Earthquake Science*, 22,  
965 425–429.
- 966 Yu, Y., Song, J., Liu, K. H., & Gao, S. S. (2015). Determining crustal structure beneath  
967 seismic stations overlying a low-velocity sedimentary layer using receiver  
968 functions. *Journal of Geophysical Research: Solid Earth*, 120.
- 969 Zelt, B. C., & Ellis, R. M. (1999). Receiver-function studies in the Trans Hudson  
970 Orogen, Saskatchewan. *Canadian Journal of Earth Sciences*, 36, 585–603.
- 971 Zhan, Y., Zhao, G., Wang, J., Xiao, Q., Tang, J. & Rokityansky, II. (2006). Crustal  
972 electric conductivity structure for Wudalianchi volcanic cluster in the  
973 Heilongjiang Province, China. *Acta Petrologica Sinica*, 22, 1494–1502.
- 974 Zhang, C., Zhang, X., Zhao, J., Liu, B., Zhang, J., Yang, Z., Hai, Y. & Sun, G. (2002).  
975 Crust–mantle structure of the Changbaishan Tianchi volcanic region and its  
976 vicinity: an exploratory study and inferences. *Chinese Journal of Geophysics*,  
977 45, 862– 871.
- 978 Zhang, F., Wu, Q., & Li, Y. (2013). The travelttime tomography study by teleseismic  
979 P wave data in the Northeast China area (in Chinese with English abstract).  
980 *Chinese Journal of Geophysics*, 56, 2690–2700.
- 981 Zhang, G., Wu, Q., Pan, J., Zhang, F., & Yu, D. (2013). Study of crustal structure and

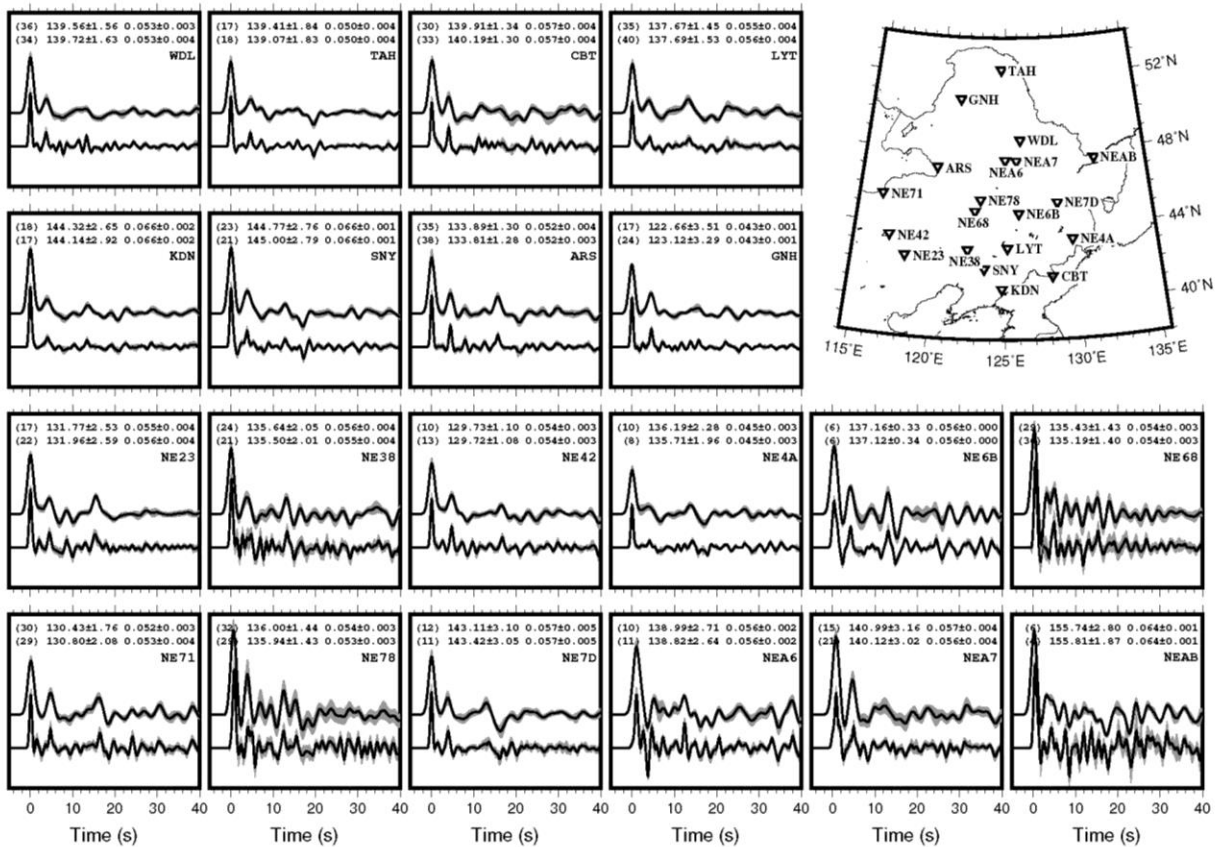
- 982 Possion ration of NE China by H-K stack and CCP stack methods (in Chinese  
983 with English abstract). *Chinese Journal of Geophysics*, 56, 4084–4094.
- 984 Zhang, J., Gao, S., Ge, W., Wu, F., Yang, J., Wilde, S. A., & Li, M. (2010).  
985 Geochronology of the Mesozoic volcanic rocks in the Great Xing'an Range,  
986 northeastern China: Implications for subduction - induced delamination.  
987 *Chemical Geology*, 276(3-4), 144–165.
- 988 Zhang, R., Wu, Q., Sun, L., He, J., & Gao, Z. (2014). Crustal and lithospheric structure  
989 of Northeast China from S - wave receiver functions. *Earth and Planetary  
990 Science Letters*, 401, 196–205.
- 991 Zhao, D., Lei, J., & Tang, R. (2004). Origin of the Changbai intraplate volcanism in  
992 Northeast China: evidence from seismic tomography, *China Science Bulletin*,  
993 49, 1401–1408.
- 994 Zhao, D., & Ohtani, E. (2009). Deep slab subduction and dehydration and their  
995 geodynamic consequences: evidence from seismology and mineral physics.  
996 *Gondwana Research*, 16, 401–413.
- 997 Zhao, D., & Tian, Y. (2013). Changbai intraplate volcanism and deep earthquakes in  
998 East Asia: A possible link? *Geophysical Journal International*, 195(2), 706–  
999 724.
- 1000 Zhao, D., Tian, Y., Lei, J., Liu, L., & Zheng, S. (2009). Seismic image and origin of  
1001 the Changbai intraplate volcano in East Asia: Role of big mantle wedge above  
1002 the stagnant Pacific slab. *Physics of the Earth and Planetary Interiors*, 173(3-  
1003 4), 197–206.
- 1004 Zhao, D., Yanada, T., Hasegawa, A., Umino, N., & Wei, W. (2012). Imaging the  
1005 subducting slabs and mantle upwelling under the Japan Island. *Geophysical  
1006 Journal International*, 190(2), 816–828.
- 1007 Zhou, J., & Wilde, S.A. (2013). The crustal accretion history and tectonic evolution of  
1008 the NE China segment of the Central Asian Orogenic Belt. *Gondwana  
1009 Research*, 23, 1365–1377.



1011

1012 Figure 1. (a) Topographic map of Northeast China and its adjacent areas, showing major  
 1013 geological features and Quaternary volcanoes (red points). Dashed black lines F1-F5  
 1014 represent the Nenjiang (NJF), Mudanjiang (MDJF), Yilan-Yitong (YYF), Dunhua-  
 1015 Mishan (DMF), and Chifeng-Kaiyuan faults (CKF), respectively. The North South

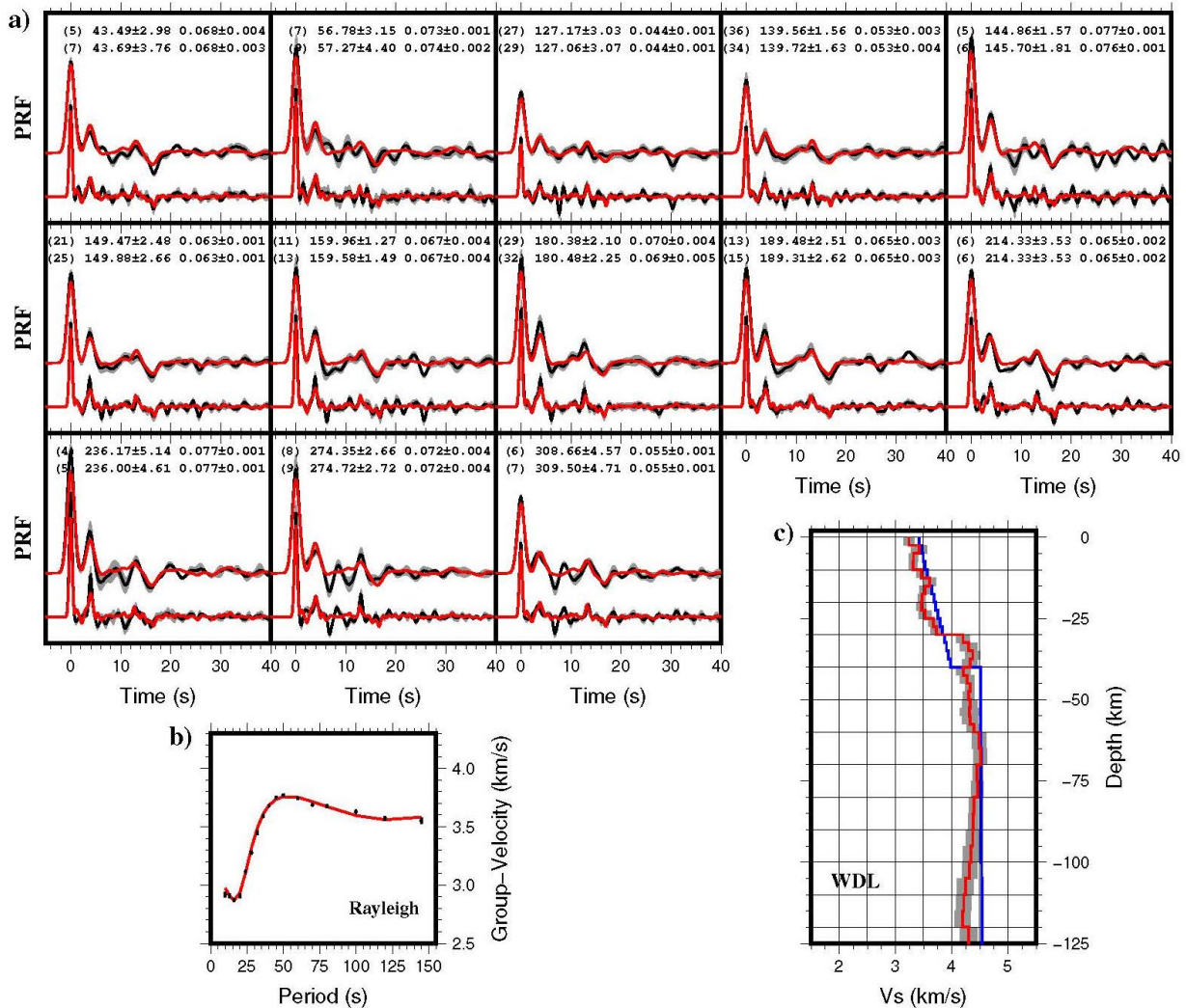
1016 Gravity Lineament (NSGL) is depicted by a dash gray line. White lines outline the main  
 1017 sedimentary basins in the region. CBM = Changbai mountains; GXM = Greater  
 1018 Xing'an mountain range; LXM = Lesser Xing'an mountain range; SJB = Sanjiang basin;  
 1019 SLB = Songliao basin; NCC = North China craton; XMOB = Xingmeng Orogenic Belt;  
 1020 CBV = Changbaishan volcano; JPHV = Jingpohu volcano; WDL CV = Wudalianchi  
 1021 volcano; HLHV = Halaha volcano; ABGV = Abaga volcano. (b) Distribution of 225  
 1022 seismic stations comprising 107 CEA permanent stations (cyan inverted triangles) and  
 1023 118 NECESSArray temporary sites (blue inverted triangles) used in our study.



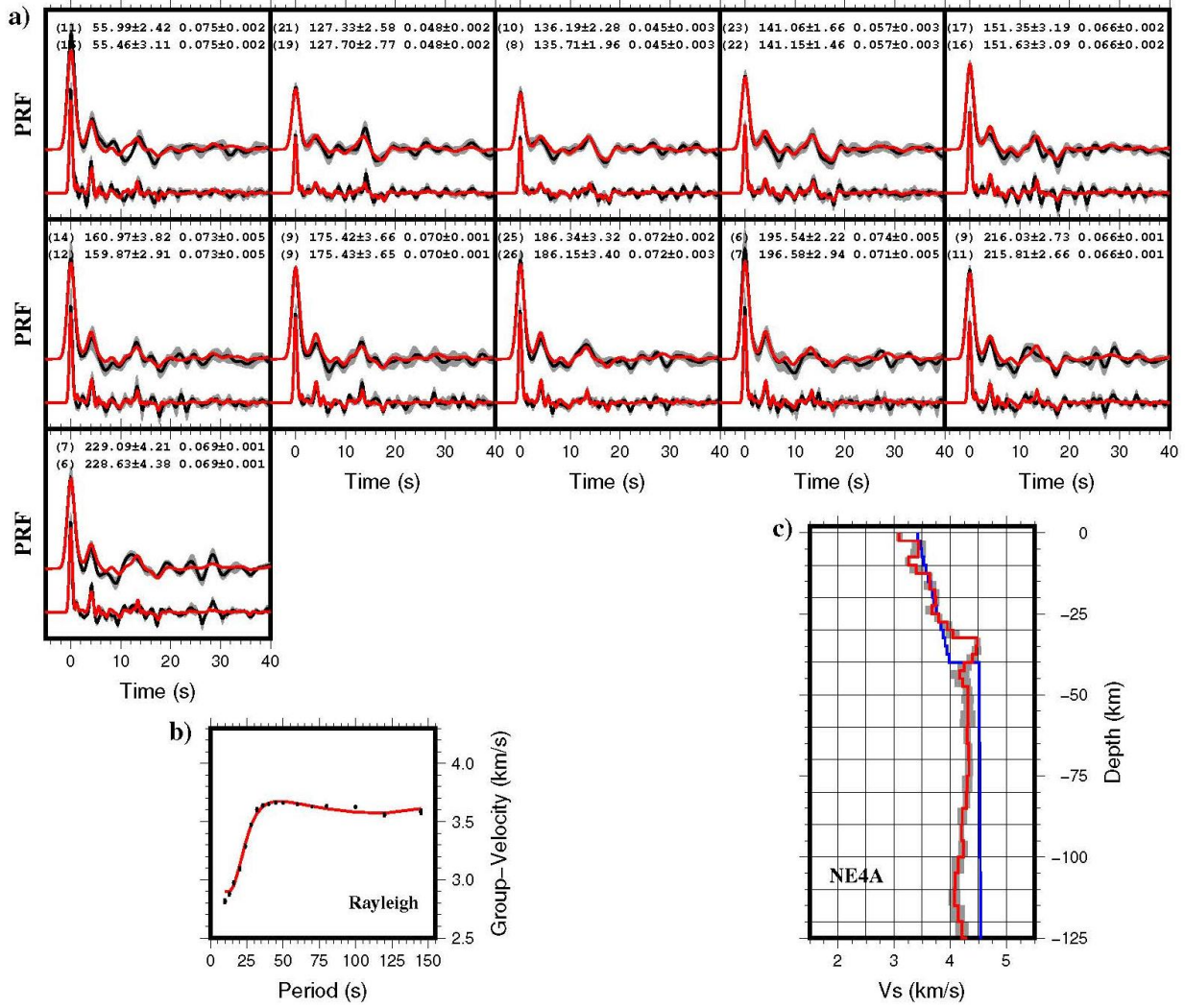
1014

1025 Figure 2. Radial receiver function averages at two Gaussian widths of  $\alpha = 1.0$  and  $2.5$   
 1026 for a small selection of stations (marked by inverted triangles in the right map). Black  
 1027 time series manifest the average receiver functions, while gray-shaded swaths indicate  
 1028 the confidence bounds. The number of receiver functions in each stack, the average  
 1029 event back-azimuth (with variation, in degree), the average ray-parameter (with

1030 variation, in second per kilometer), and the station name are shown in each panel.

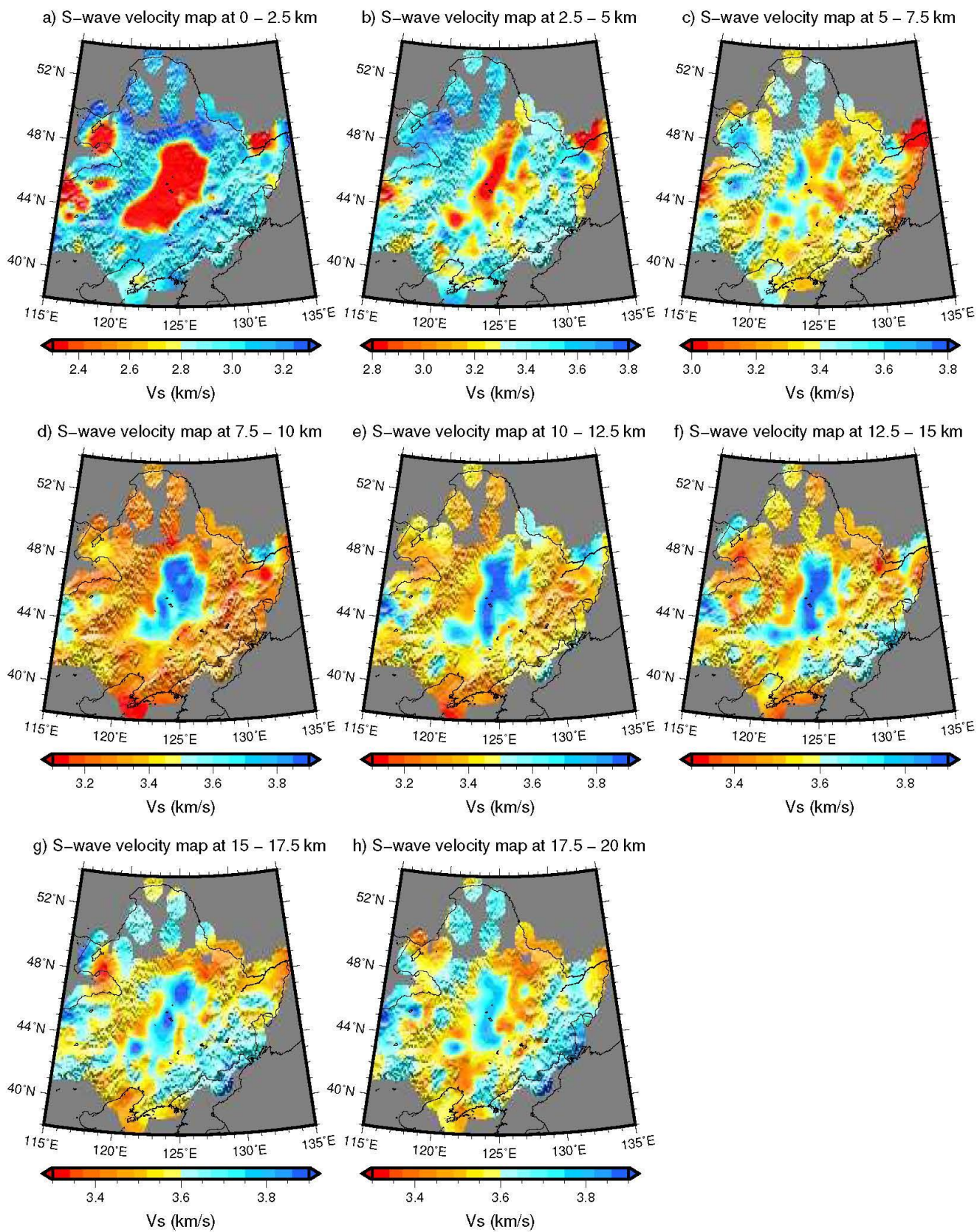


1031  
 1032 Figure 3. Joint inversion of receiver function averages and Rayleigh wave group  
 1033 velocities at station WDL. In panels (a), black and red lines represent the observed (with  
 1034 gray-shaded confidence bounds) and predicted receiver functions, respectively. The  
 1035 number of receiver functions for each cluster, the average back-azimuth (with variation,  
 1036 in degree), and the average ray-parameter (with variation, in second per kilometer) are  
 1037 exhibited. The observed and predicted Rayleigh wave group velocities (period range 10  
 1038 to 145 s) are represented by black points and red curve in panel (b). The 1-D inverted  
 1039 shear-wave velocity model (red, with gray-shaded confidence bounds) and the initial  
 1040 model (blue) are visualized in panel (c).



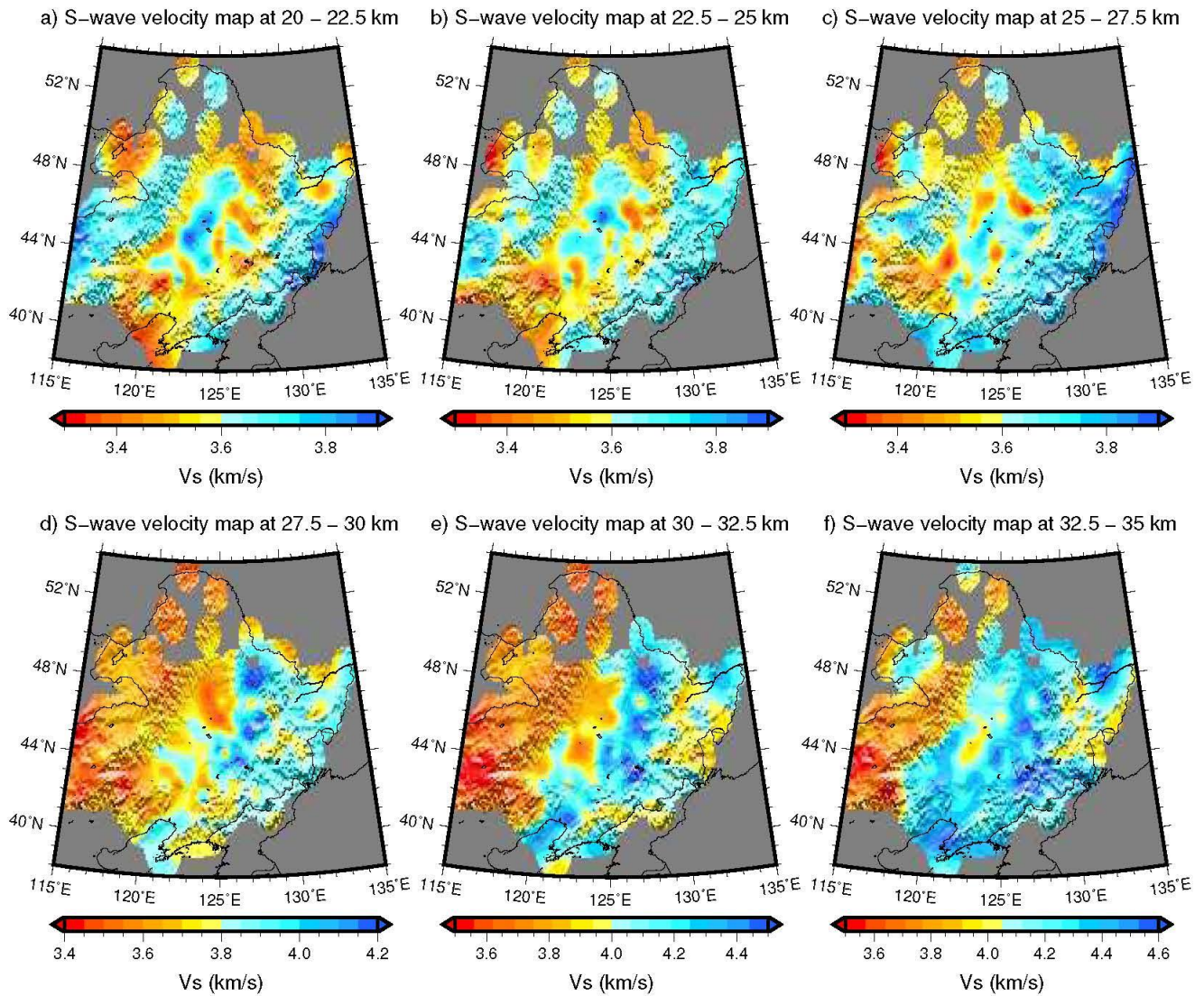
10..

1042 Figure 4. Same as Figure 3 but for station NE4A.

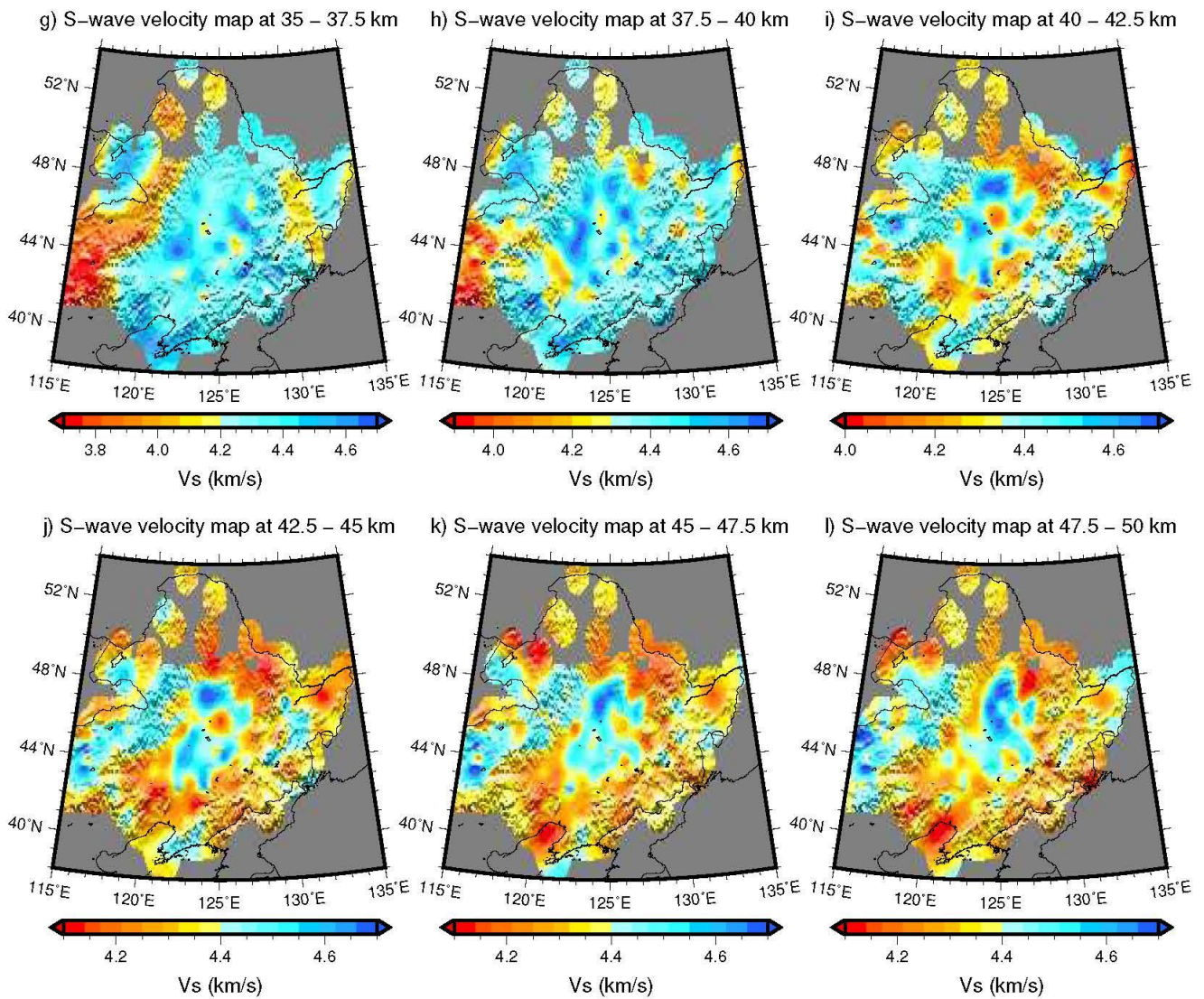


1044 Figure 5. Horizontal slices of shear-wave velocities at upper-crustal depths (0-20 km)

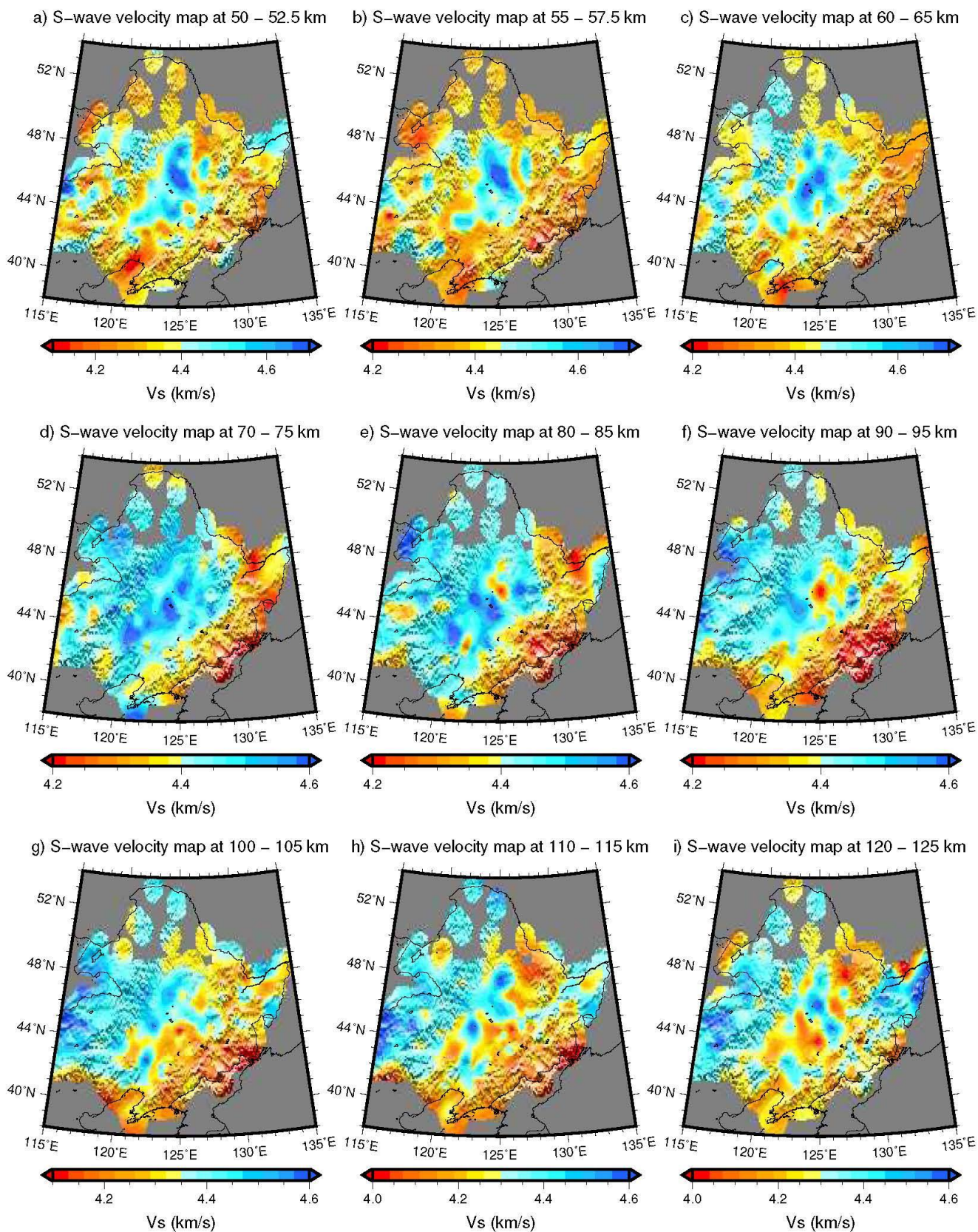
1045 beneath Northeast China. Note that color scale changes for each map to enhance lateral  
1046 velocity contrasts.



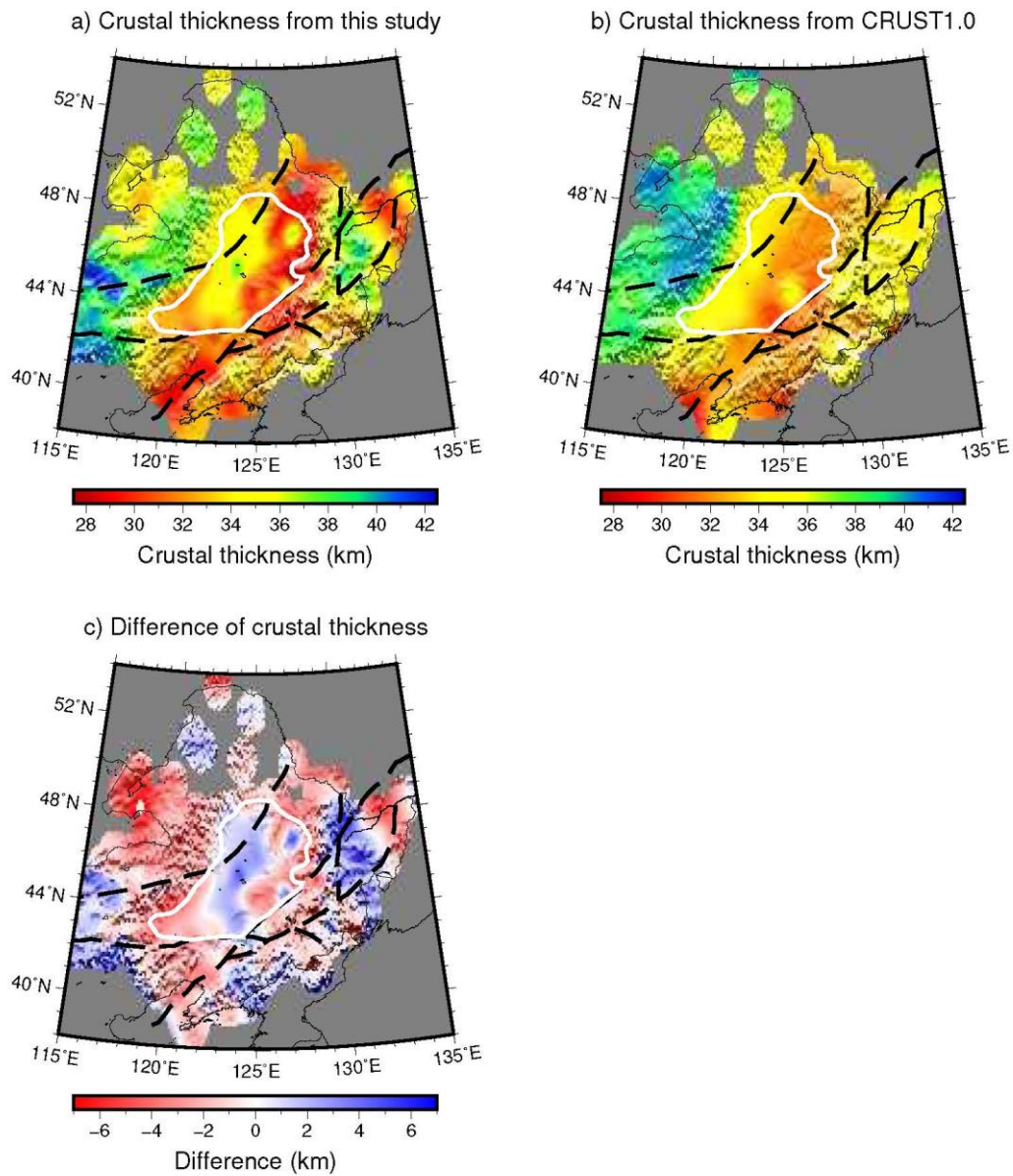
1048 Figure 6. Horizontal slices of S-wave velocities at lower-crustal and Moho depths (20-  
1049 50 km) below Northeast China.



1051 Figure 6 (continued).



1053 Figure 7. Horizontal slices of S-wave velocities at upper-mantle depths (50-125 km).

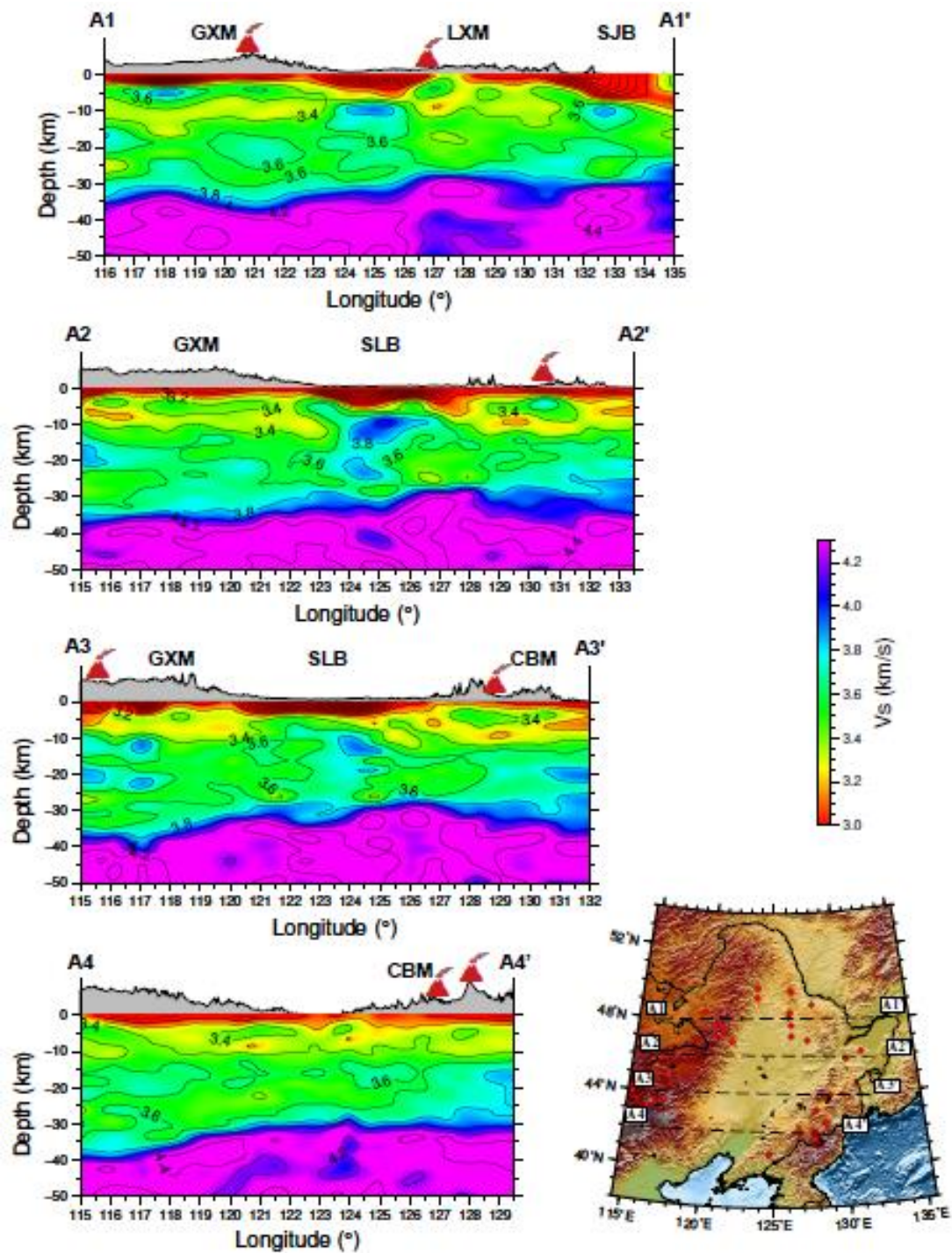


1054

1055 Figure 8. Comparison of the crustal thickness map obtained in this study with the crustal

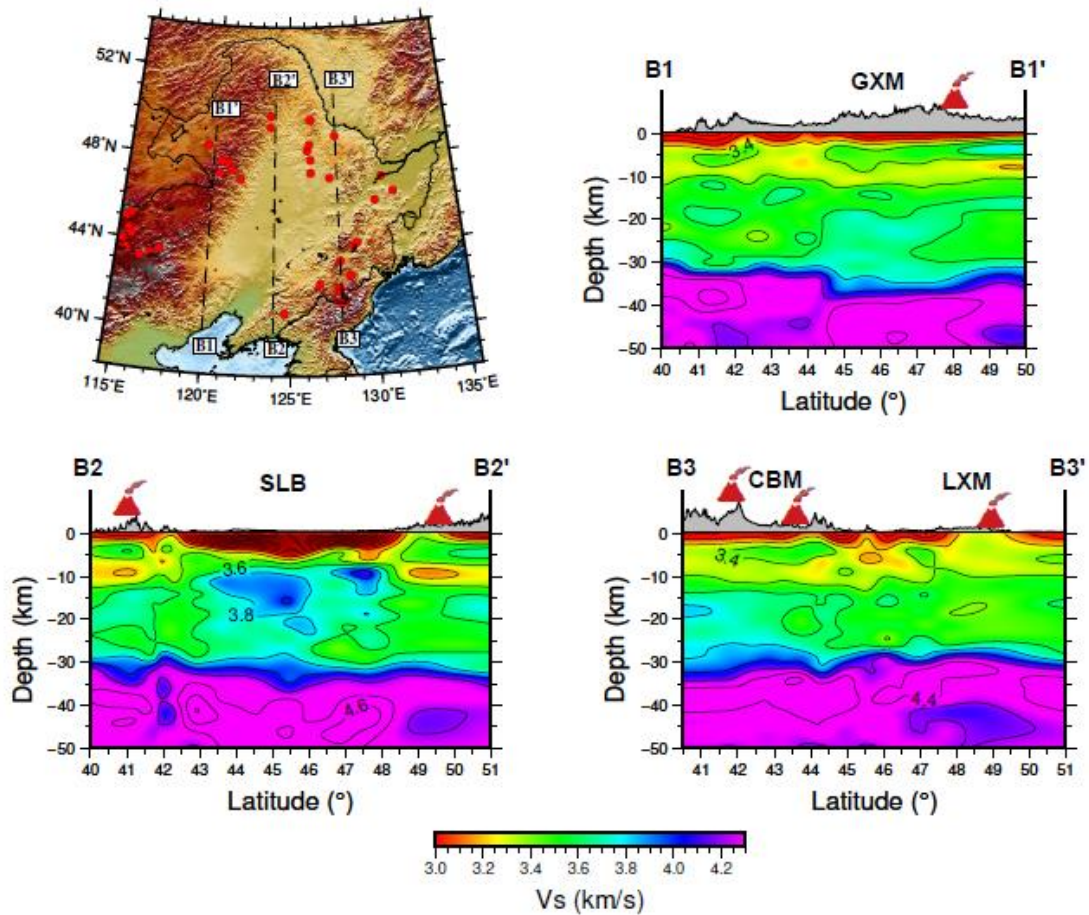
1056 thickness from CRUST1.0. Panel c shows the differences between our results and

1057 CRUST1.0.



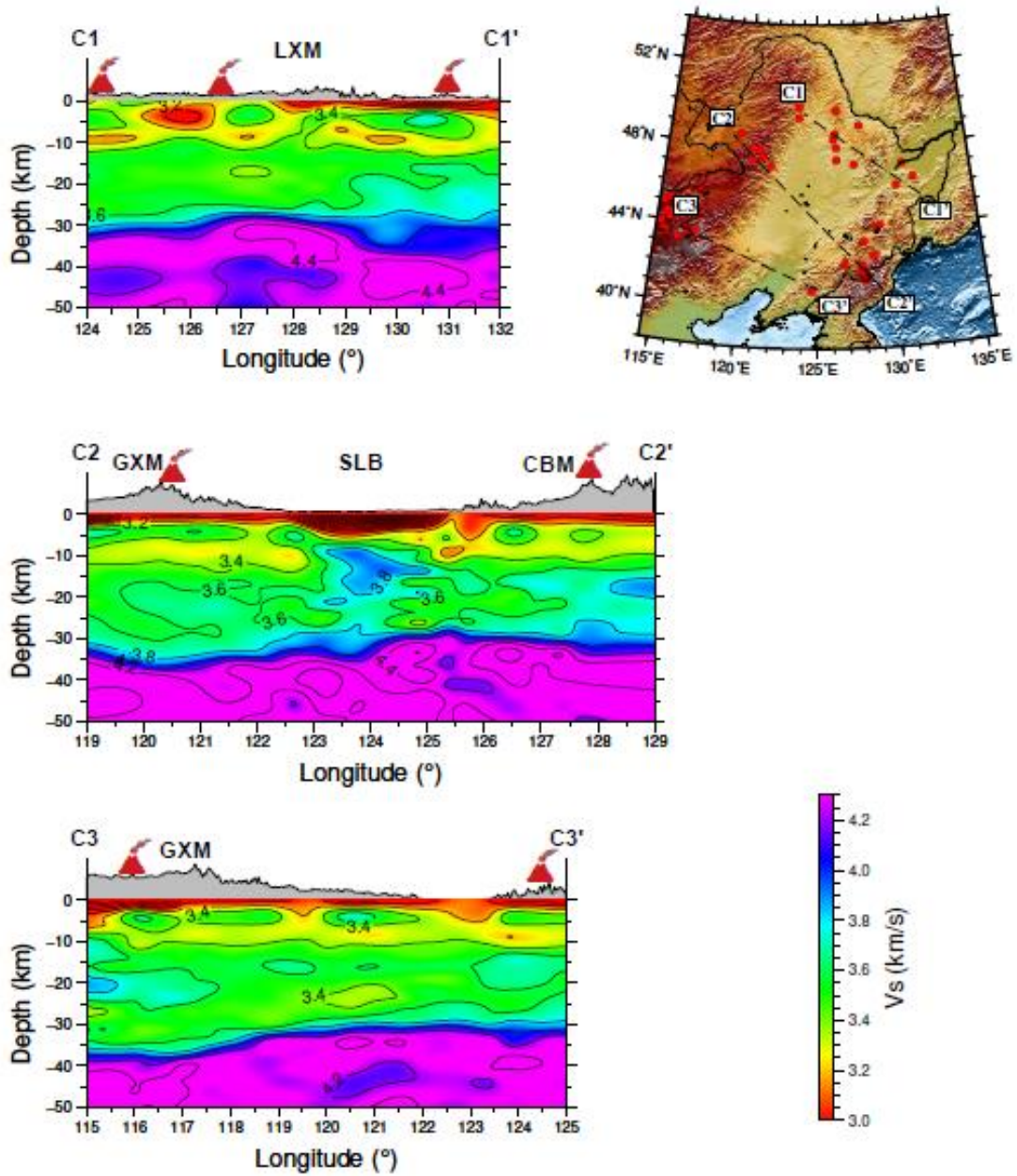
1058

1059 Figure 9. Vertical slices of shear-wave velocity along profiles A1–A4 across Northeast  
 1060 China over the crustal depths (0–50 km). Red points in the map indicate Quaternary  
 1061 volcanoes. CBM = Changbai mountains; GXM = Greater Xing’an mountain range;  
 1062 LXM = Lesser Xing’an mountain range; SJB = Sanjiang basin; SLB = Songliao basin.



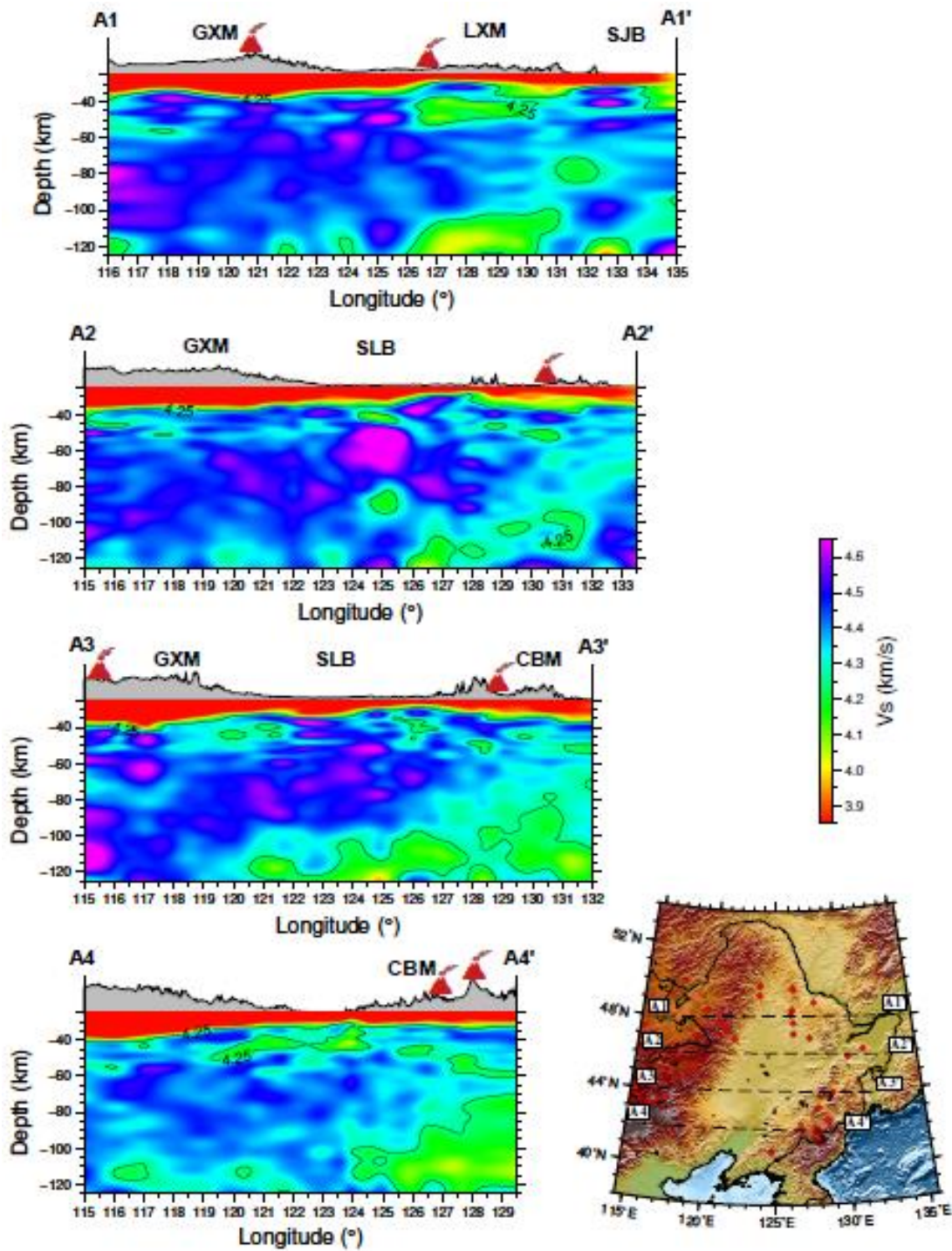
1063

1064 Figure 10. Vertical transects through the shear-wave velocity model along profiles B1–  
 1065 B3 across Northeast China for the crustal levels (0–50 km). Red points in the map  
 1066 represent Quaternary volcanoes. CBM = Changbai mountains; GXM = Greater Xing’an  
 1067 mountain range; LXM = Lesser Xing’an mountain range; SLB = Songliao basin.



1068

1069 Figure 11. Vertical shear-wave velocity transects along profiles C1–C3 over the depth  
 1070 range of 0–50 km. Quaternary volcanoes are marked as red points in the map. CBM =  
 1071 Changbai mountains; GXM = Greater Xing’an mountain range; LXM = Lesser Xing’an  
 1072 mountain range; SLB = Songliao basin.



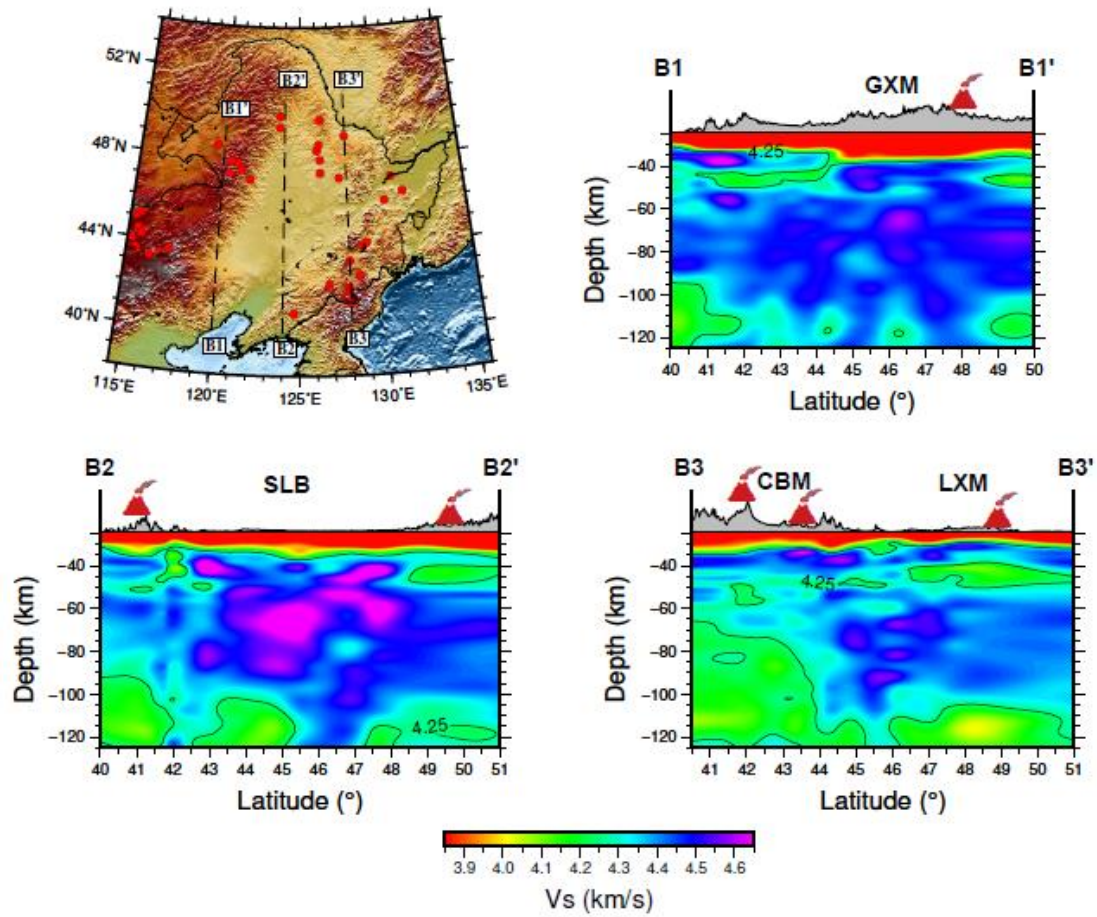
1073

1074 Figure 12. Vertical slices of S-wave velocity along profiles A1–A4 across the study area

1075 over the upper-mantle depths (25–125 km). CBM = Changbai mountains; GXM =

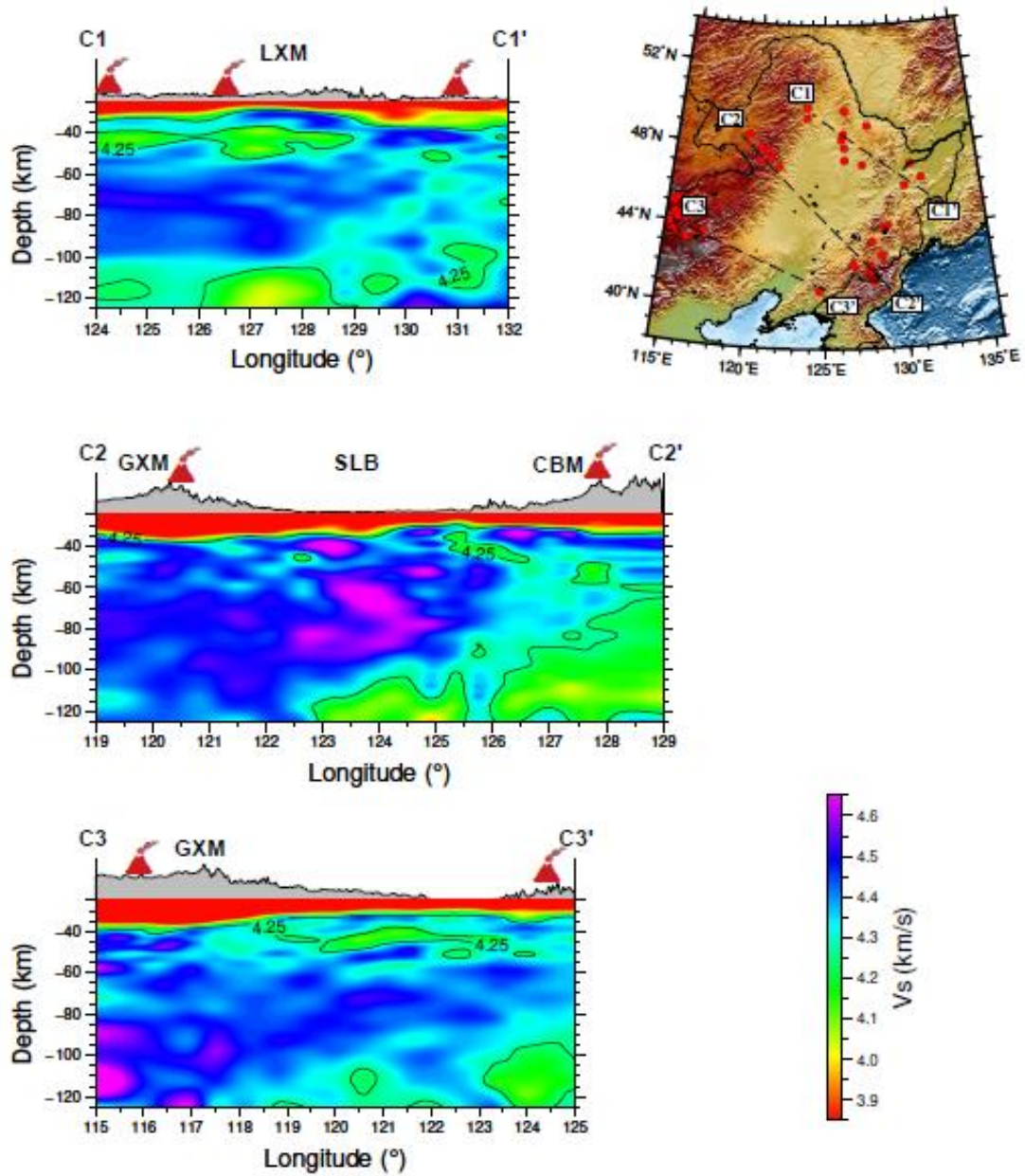
1076 Greater Xing’an mountain range; LXM = Lesser Xing’an mountain range; SJB =

1077 Sanjiang basin; SLB = Songliao basin.



1078

1079 Figure 13. Vertical slices of shear-wave velocity along profiles B1–B3 across the study  
 1080 area over the upper mantle (25–125 km). CBM = Changbai mountains; GXM = Greater  
 1081 Xing’an mountain range; LXM = Lesser Xing’an mountain range; SLB = Songliao  
 1082 basin.

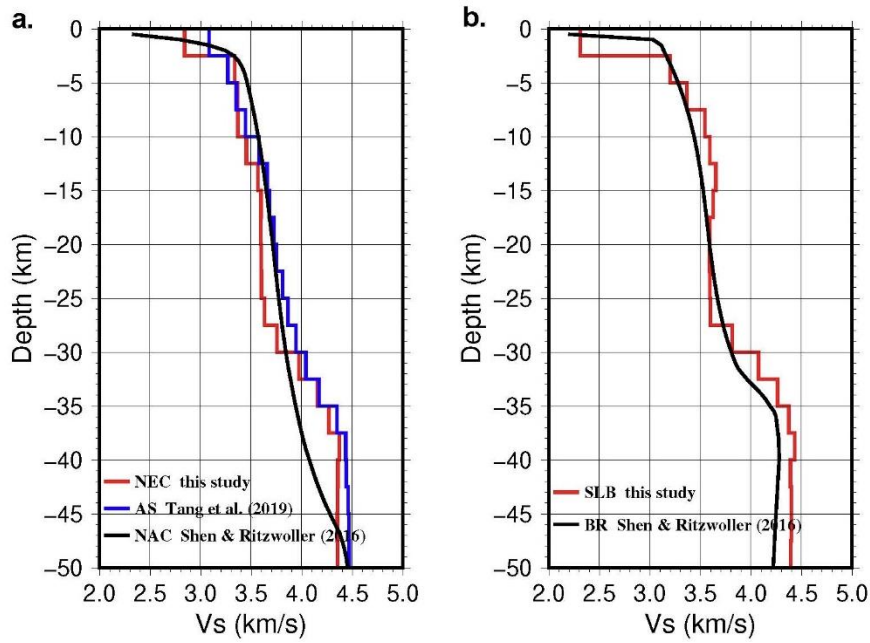


1083

1084 Figure 14. Vertical transects of S-wave velocity along profiles C1–C3 over the depth

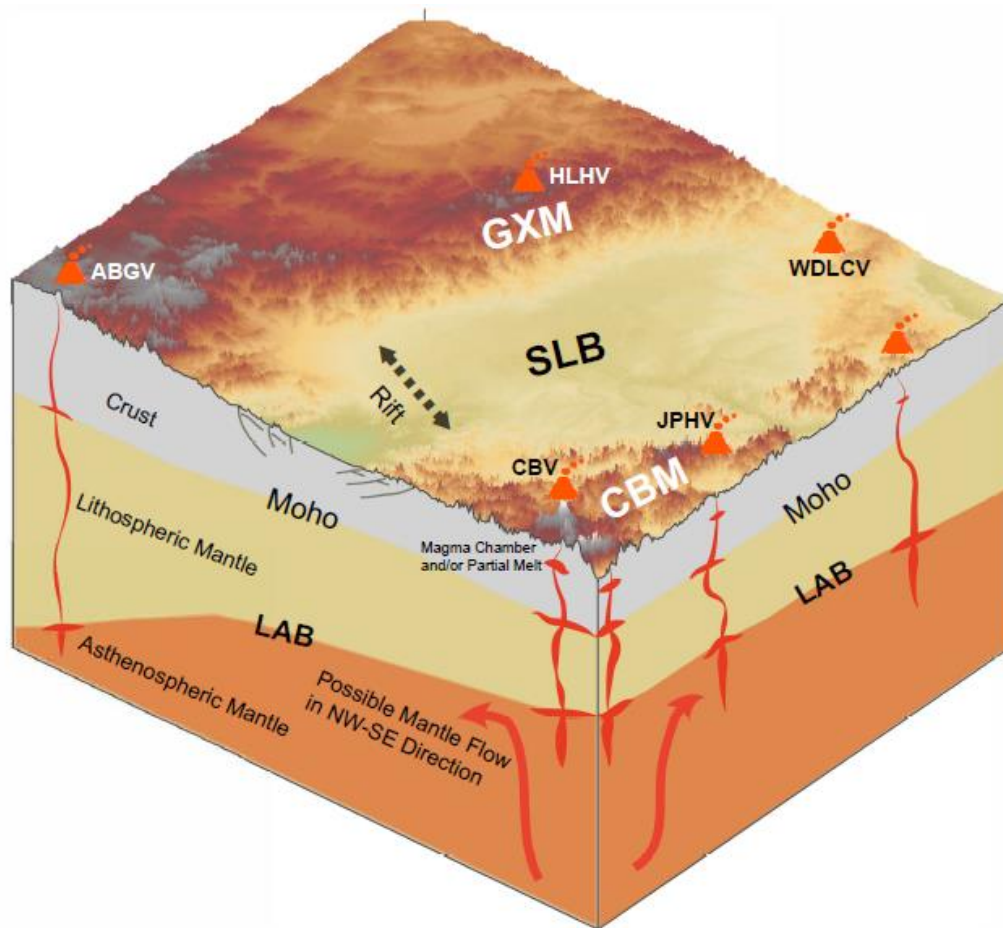
1085 range of 25–125 km. CBM = Changbai mountains; GXM = Greater Xing’an mountain

1086 range; LXM = Lesser Xing’an mountain range; SLB = Songliao basin.



1087

1088 Figure 15. (a) 1-D average shear wave velocity structure beneath Northeast China (NEC,  
 1089 red line), the Arabian shield (AS, blue line, Tang et al., 2019), and the North American  
 1090 craton (NAC, black line, Shen & Ritzwoller, 2016). (b) 1-D average S-velocity model  
 1091 below the Songliao basin (SLB, red line) and the Basin and Range (BR, black line, Shen  
 1092 & Ritzwoller, 2016) in Western United States.



1093

1094 Figure 16. 3-D schematic diagram across the study area, showing the main structural  
 1095 features such as the lithospheric thickening westward, and the proposed Cenozoic  
 1096 volcanic/magmatic mechanism at lithospheric and sub-lithospheric levels below  
 1097 Northeast China. CBM = Changbai mountains; GXM = Greater Xing'an mountain  
 1098 range; SLB = Songliao basin; CBV = Changbaishan volcano; JPHV = Jingpohu volcano;  
 1099 WDL CV = Wudalianchi volcano; HLHV = Halaha volcano; ABGV = Abaga volcano;  
 1100 LAB = lithosphere-asthenosphere boundary.